ACS NANO
Cite This: ACS Nano 2020, 14, 185−195
www.acsnano.org

ARTICLE

Discovery of Stable and Selective Antibody Mimetics from Combinatorial Libraries of Polyvalent, Loop-Functionalized Peptoid Nanosheets

Jae Hong Kim,[†,#] Samuel C. Kim,[‡,#] Mark A. Kline,[†] Elissa M. Grzincic,[†] Blakely W. Tresca,[†] Joshua Cardiel,[‡] Mohsen Karbaschi,[‡] Dilani C. Dehigaspitiya,[§] Yulin Chen,[∥] Venkatareddy Udumula,[∥] Tengyue Jian,[∥] Daniel J. Murray,[†] Lisa Yun,[†] Michael D. Connolly,[†] Jianfang Liu,[†] Gang Ren,[†] Chun-Long Chen,[∥] Kent Kirshenbaum,[§] Adam R. Abate,[*,‡,⊥] and Ronald N. Zuckermann[*,†]

[†]The Molecular Foundry, Lawrence Berkeley National Laboratory, Berkeley, California 94720, United States
[‡]Department of Bioengineering and Therapeutic Sciences, University of California, San Francisco, San Francisco, California 94158, United States
[§]Department of Chemistry, New York University, New York, New York 10003, United States
[∥]Physical Sciences Division, Pacific Northwest National Laboratory, Richland, Washington 99352, United States
[⊥]Chan Zuckerberg Biohub, San Francisco, California 94158, United States

Supporting Information

ABSTRACT: **The ability of antibodies to bind a wide variety of analytes with high specificity and high affinity makes them ideal candidates for therapeutic and diagnostic applications. However, the poor stability and high production cost of antibodies have prompted exploration of a variety of synthetic materials capable of specific molecular recognition. Unfortunately, it remains a fundamental challenge to create a chemically diverse population of protein-like, folded synthetic nanostructures with defined molecular conformations in water. Here we report the synthesis and screening of combinatorial libraries of sequence-defined peptoid polymers engineered to fold into ordered, supramolecular nanosheets displaying a high spatial density of diverse, conformationally constrained peptoid loops on their surface. These polyvalent, loop-functionalized nanosheets were screened using a homogeneous Förster resonance energy transfer (FRET) assay for binding to a variety of protein targets. Peptoid sequences were identified that bound to the heptameric protein, anthrax protective antigen, with high avidity and selectivity. These nanosheets were shown to be resistant to proteolytic degradation, and the binding was shown to be dependent on the loop display density. This work demonstrates that key aspects of antibody structure and function—the creation of multivalent, combinatorial chemical diversity within a well-defined folded structure—can be realized with completely synthetic materials. This approach enables the rapid discovery of biomimetic affinity reagents that combine the durability of synthetic materials with the specificity of biomolecular materials.**

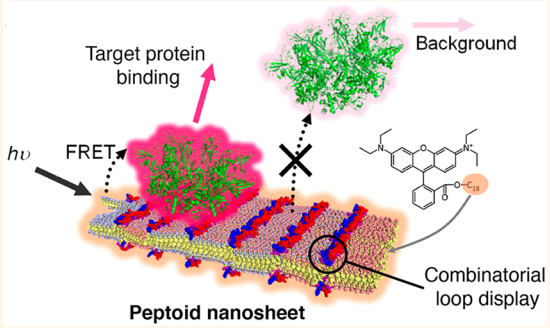

KEYWORDS: *protein-mimetic materials, multivalent molecular recognition, combinatorial display, two-dimensional nanomaterials, bioinspired polymers*

Antibodies naturally act as molecular recognition elements having high specificity and affinity to their corresponding antigens. While antibodies are nature's ultimate pathogen detectors, their utility for biomedical applications is restricted by high production cost, low solubility, loss of activity due to improper folding, and difficulties with chemical modification.[1,2] To avoid these drawbacks and to emulate these antibodies, various synthetic biomacromolecules have been developed by rational design and combinatorial approaches using natural scaffolds, such as proteins, nucleic

Received: September 23, 2019
Accepted: November 21, 2019
Published: December 2, 2019

Downloaded via LAWRENCE BERKELEY NATL LABORATORY on April 17, 2020 at 06:00:45 (UTC).
See https://pubs.acs.org/sharingguidelines for options on how to legitimately share published articles.

© 2019 American Chemical Society

DOI: 10.1021/acsnano.9b07498
ACS Nano 2020, 14, 185−195

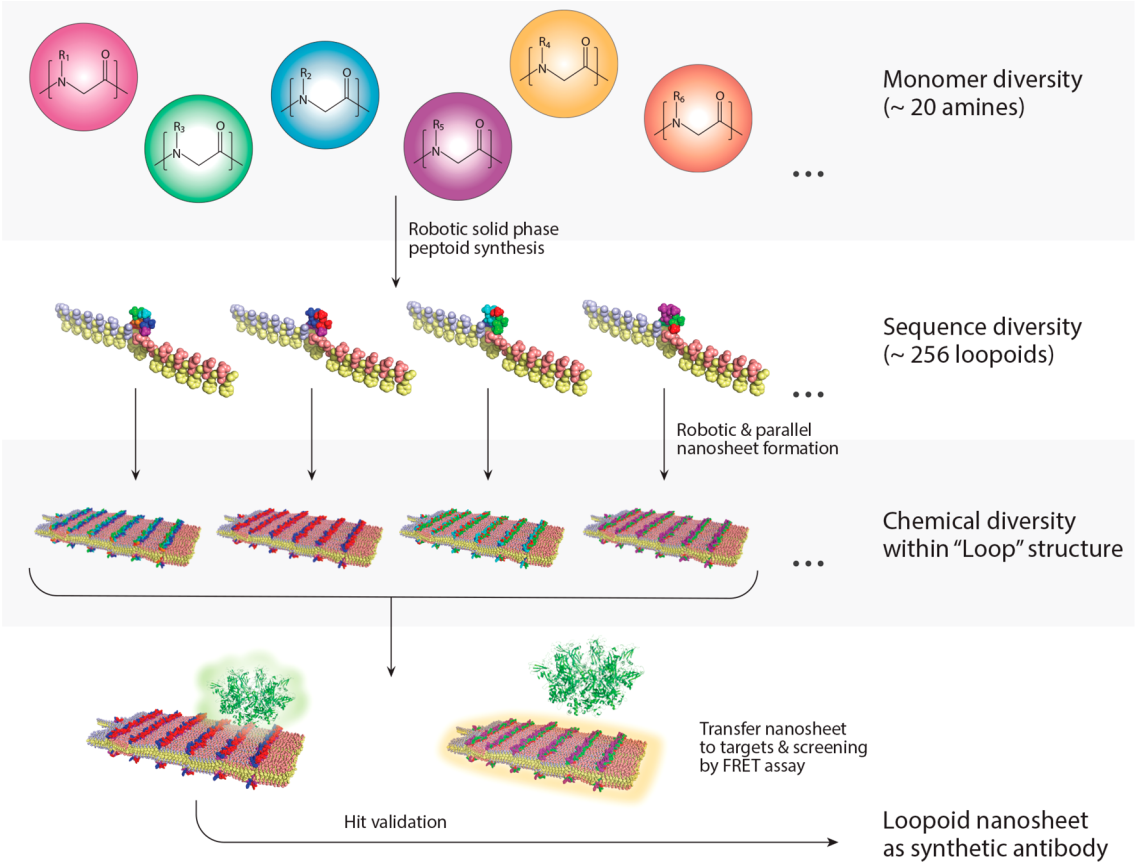

Figure 1. Combinatorial discovery of loop-functionalized peptoid nanosheets as chemically diverse, biomimetic affinity reagents. The hierarchical assembly creates polyvalent chemical diversity within a conformationally constrained, folded context.

acids, and bacterial phages.[3,4] These approaches mimic, all in some way, the sophisticated three-dimensional structures of antibody binding, in which multiple, diverse chemical functionalities are presented in precise spatial geometries. However, the process for discovering artificial affinity reagents is laborious due to the requisite iterative hit selection and amplification; moreover, their low stability against proteases and poor binding affinities in the micromolar range limit the utility of these materials. Antibody mimetics discovered by combinatorial approaches have been spotlighted due to their robustness and binding affinities,[5,6] but are limited in chemical diversity and their ability to display complex, folded, binding structures. Thus, there is an unmet need for methods enabling the facile and rapid discovery of molecularly defined synthetic antibodies consisting of entirely non-natural, robust materials.

Peptoids are bioinspired and sequence-defined *N*-substituted glycine polymers. They are ideal as building blocks for constructing protein-like architectures, because their sequence-defined linear chains can reproducibly fold into specific molecular architectures due to assorted long-range inter- and intramolecular noncovalent interactions.[7−14] They are efficiently synthesized by the automated solid-phase submonomer method, using diverse and readily available amine synthons, to precisely modulate chain length, monomer sequence, and side chain chemistry. Like proteins, this provides the opportunity to program both folding information and biological activity into the chemical sequence of the polymer chain.[15,16] The free-floating 2-dimensional nanosheet is a fascinating example of a folded peptoid-based nanomaterial with atomically defined structure.[17] In this work, we mimic the basic structure of the antibody binding site by positioning a diversity of well-defined peptoid loops on the surface of peptoid nanosheets. These nanosheets are made from the self-assembly of peptoid 42-mer strands that contain a central and variable chemically diverse hexameric loop domain, flanked by two fixed nanosheet-forming domains.[18,19] Atomic force microscopy (AFM) and protein binding experiments show that these loops are displayed on the nanosheet surface.[18,19] Specific binding affinity for target proteins can be encoded by the monomer sequence of the loop-display domain, highlighting its potential as a biologically relevant binding material. Furthermore, nanosheet self-assembly is triggered by interfacial compression of the air−water interface,[20] allowing the composition of the loops to be controlled prior to sheet formation. The zwitterionic surface of peptoid nanosheets also makes them an optimal chassis for display of functional loops, since it prevents nonspecific adhesion of biomolecules.[21]

An important structural feature of loop-functionalized peptoid nanosheets is the opportunity to enable multivalent interactions with substrates due to their high spatial density of loops on the surface.[20] The ability of these high-surface-area materials to support multiple binding events simultaneously boosts selectivity and sensitivity for target proteins among various biomacromolecules.[22] Furthermore, antibody-like peptoid nanosheets resist degradation by proteases, solvents, and extreme pH and temperature conditions, because they lack peptide bonds in their backbone structure.[16,23,24] They can be engineered to employ photoreactive monomers for cross-linking the nanosheet interior, yielding increased chemical and mechanical stability.[25] While peptoid nanosheets thus provide

DOI: 10.1021/acsnano.9b07498
ACS Nano 2020, 14, 185−195

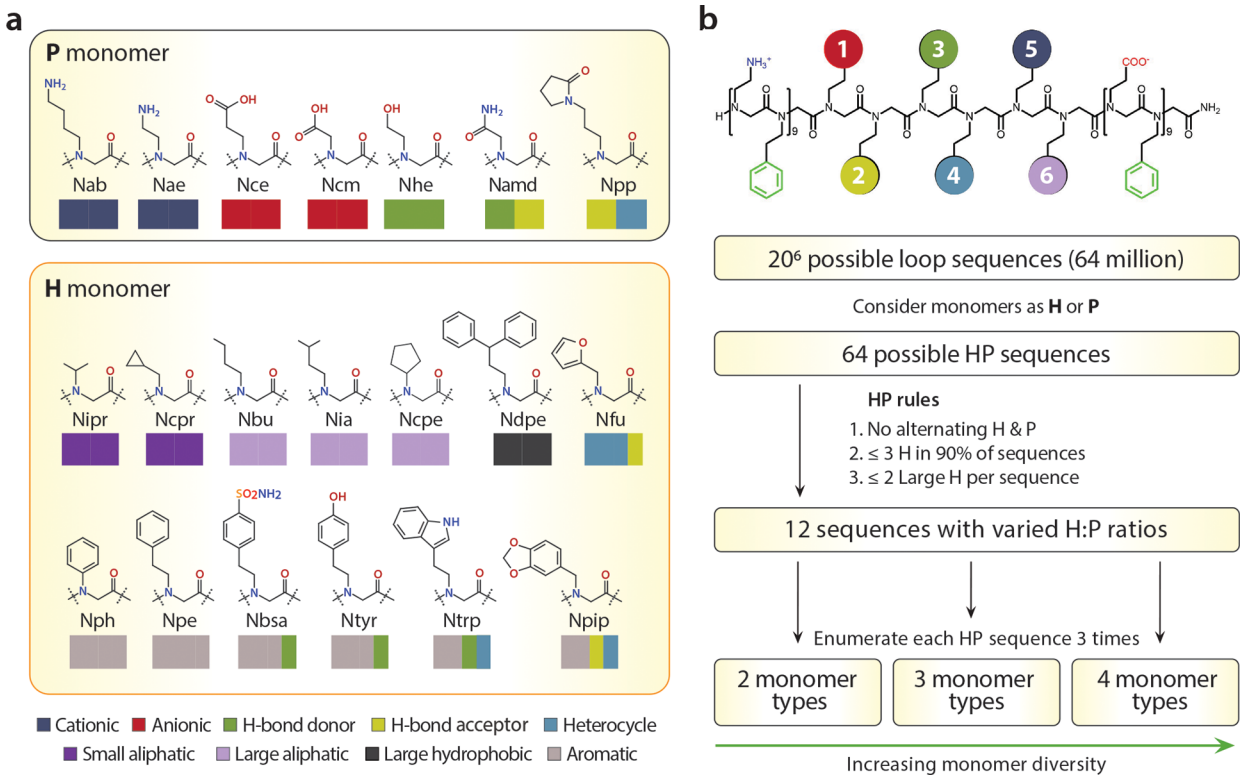

Figure 2. Design of the chemically diverse binding loops, built from a basis of 20 efficiently incorporated monomers. (a) P (hydrophilic) and H (hydrophobic) amine monomers exhibiting various properties. Colored rectangles represent primary and secondary properties of monomers. All abbreviations of monomers are included in Supporting Information. (b) Design algorithm for creating a maximally diverse set of loop insert sequences, while avoiding extremes of hydrophobicity.

valuable chemical and structural properties as affinity reagents, missing from the toolkit is a process for mimicking the recombination and affinity maturation of antibodies, which is critical to the immune system's ability to obtain specific and high affinity binders to targets. If chemists could develop an *in vitro* approach for generating specific, high affinity nanosheet binders to unfamiliar targets, these synthetic materials could overcome many of the drawbacks of antibodies.

Herein, we describe a general approach for the rapid discovery of biomimetic affinity reagents by the screening of combinatorial libraries of chemically diverse, loop-functionalized peptoid nanosheets. The discovery cycle comprised four major steps: the chemical synthesis of loop-containing peptoids (loopoids), the supramolecular assembly of loopoid nanosheets, the screening of the loopoid nanosheets against various proteins for binding activity (hits), and hit validation (Figure 1). First, the loopoid strands, which are based on a block-patterned 36-mer nanosheet-forming sequence, with the insertion of six monomers in the middle to form a conformationally rigidified surface-displayed loop, were synthesized robotically using the automated solid phase submonomer method. Drawing upon a set of 20 chemically diverse peptoid monomers, we produced a library of 256 individual loopoid strands. We then employed an autopipetting robot to initiate the supramolecular assembly of nanosheets in a high-throughput, parallel manner from the loopoids in multiwell plates. The assembled loopoid nanosheets were then used directly in a variety of target protein binding assays based on a Förster resonance energy transfer (FRET) assay.[20] On the basis of this automated process for synthesis and screening, we discovered a nanosheet binder for anthrax protective antigen [$(PA63)_7$], a ring-shaped homoheptameric toxin-related protein. On the basis of the chemical properties of the hit loop sequences, we identify rules for understanding the specific binding of loopoid nanosheets to $(PA63)_7$. We also demonstrated the importance of multivalency in hit interactions by biolayer interferometry, electron microscopy, and fluorescence imaging and FRET analyses.

RESULTS AND DISCUSSION

Design of Loopoid Libraries. The diverse antigenic specificity of antibodies is achieved by the chemical diversity (*i.e.*, combination of 20 amino acids) within the structural context of complementarity-determining regions (CDR). To replicate the binding specificity of antibodies to their corresponding antigens, the loop-functionalized nanosheet is an ideal scaffold because of the opportunity to display chemically diverse moieties within a conformationally constrained loop domain projected from the nanosheet polar surface. For these displayed loops, we identified a set of 7 hydrophilic (**P**) and 13 hydrophobic (**H**) peptoid monomers possessing distinct chemical properties similar to natural amino acids (Figure 2a). Combinatorial loop libraries were designed to contain specific combinations of **H** and **P** monomers to avoid extremes of hydrophobicity or charge within the loop domains. These combinations were selected using design rules based on monomer chemical properties, the feasibility of polypeptoid synthesis, and its capacity to fold into nanosheets (Figure 2b). We fixed the length of the loop domain to be six monomers in order to protrude far enough from the surface of nanosheets for efficient protein binding.[20] A peptoid loop six monomers in length is expected to have conformational rigidity, as has been shown in similarly sized peptoid macrocycles.[26] There are 64

DOI: 10.1021/acsnano.9b07498
ACS Nano 2020, 14, 185−195

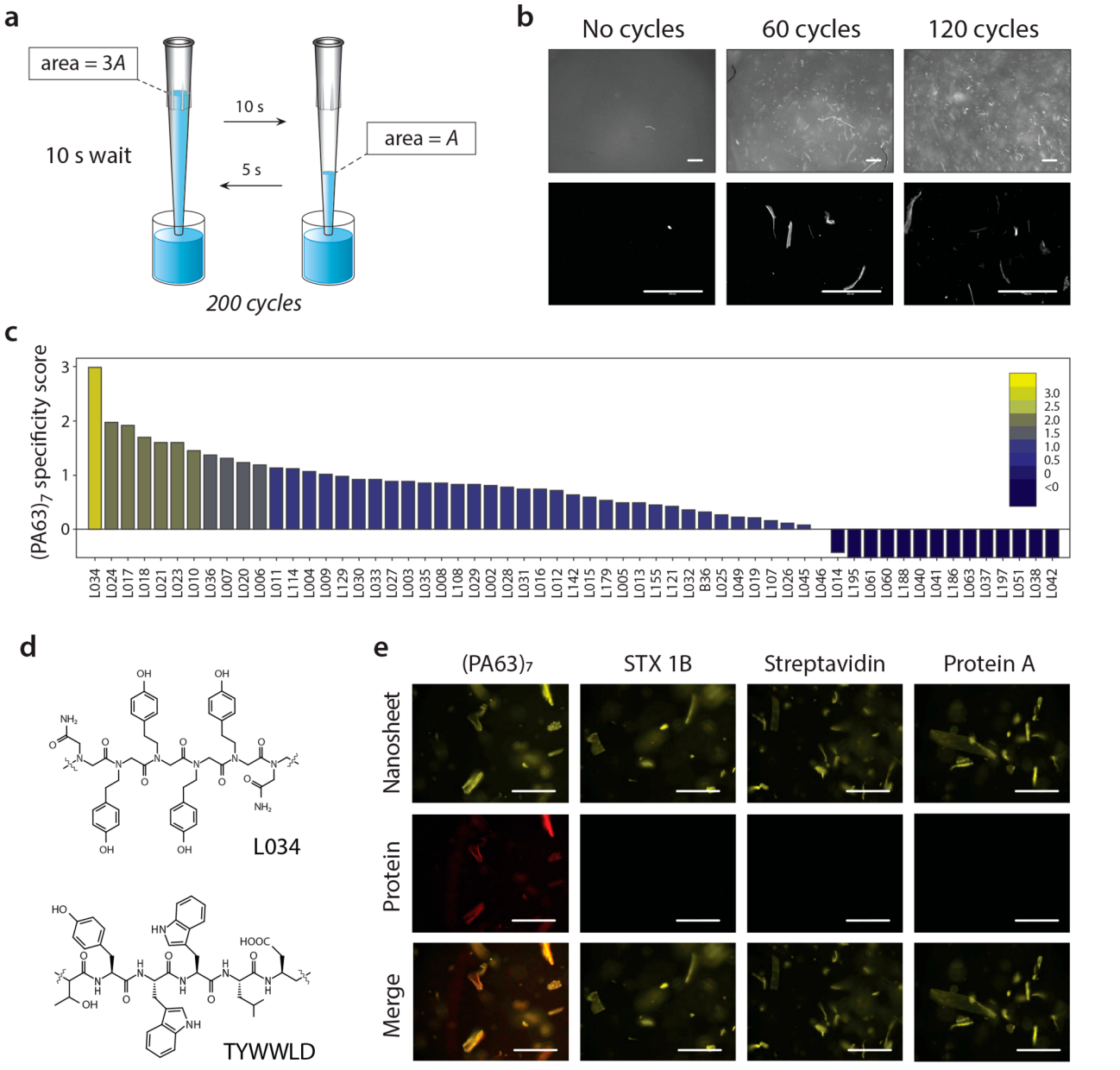

Figure 3. Automated production and screening of a loop-functionalized peptoid nanosheet library for specific binding to $(PA63)_7$. (a) Schematic illustration of peptoid nanosheet formation by interfacial compression through robotic pipetting. (b) Fluorescence microscopic images of pipetting-induced peptoid nanosheets. All scale bars represent 100 μm. (c) $(PA63)_7$ specificity score of various loopoid nanosheets from screening process. The detail of the calculation of specificity score described in Supporting Information. (d) Chemical structure of loop domain of L034 and TYWWLD nanosheet. (e) Validation of $(PA63)_7$ binding specificity of L034 nanosheet by fluorescent microscopy. All scale bars represent 100 μm.

possible amphiphilic **HP** patterns of loop sequence in a 6-mer by considering only the **H** and **P** property of monomers. Our previous studies determined that the nanosheet formation mechanism involves a key intermediate where the peptoids must adsorb to the air−water interface to form an ordered monolayer.[18] Hence, the overall water solubility and surface activity must be balanced to promote self-assembly and the correct folding of loops on the surface of nanosheets. For this reason, we eliminated sequences with alternating **H** and **P** monomers, sequences with ≥3 **H** monomers, and sequences with ≥2 large **H** monomers per sequence. Employing these rules, we randomly selected 12 hexameric **HP** patterns. Chemical diversity was introduced into the loop sequence by classifying each monomer according to their primary and secondary chemical characteristics: aromatic, small aliphatic, large aliphatic, large hydrophobic, cationic, anionic, hydrogen bond donor/acceptor, and heterocycle. Considering the chemical characteristics of these monomers, the 12 initial **HP** patterns were enumerated to a set of 256 specific sequences with a bias toward minimizing the number of different monomers within the same sequence. In this way the chemical distinctness of each loop could be maximized, making it easier to later identify key chemical properties essential for molecular recognition (Supporting Information, Table S1).

Screening of Loopoid Library and Hit Validation. The first hurdle to discovering a nanosheet affinity reagent is to effectively convert the library of individual peptoid chains into loop-functionalized nanosheet libraries. Conventionally, this

DOI: 10.1021/acsnano.9b07498
ACS Nano 2020, 14, 185−195

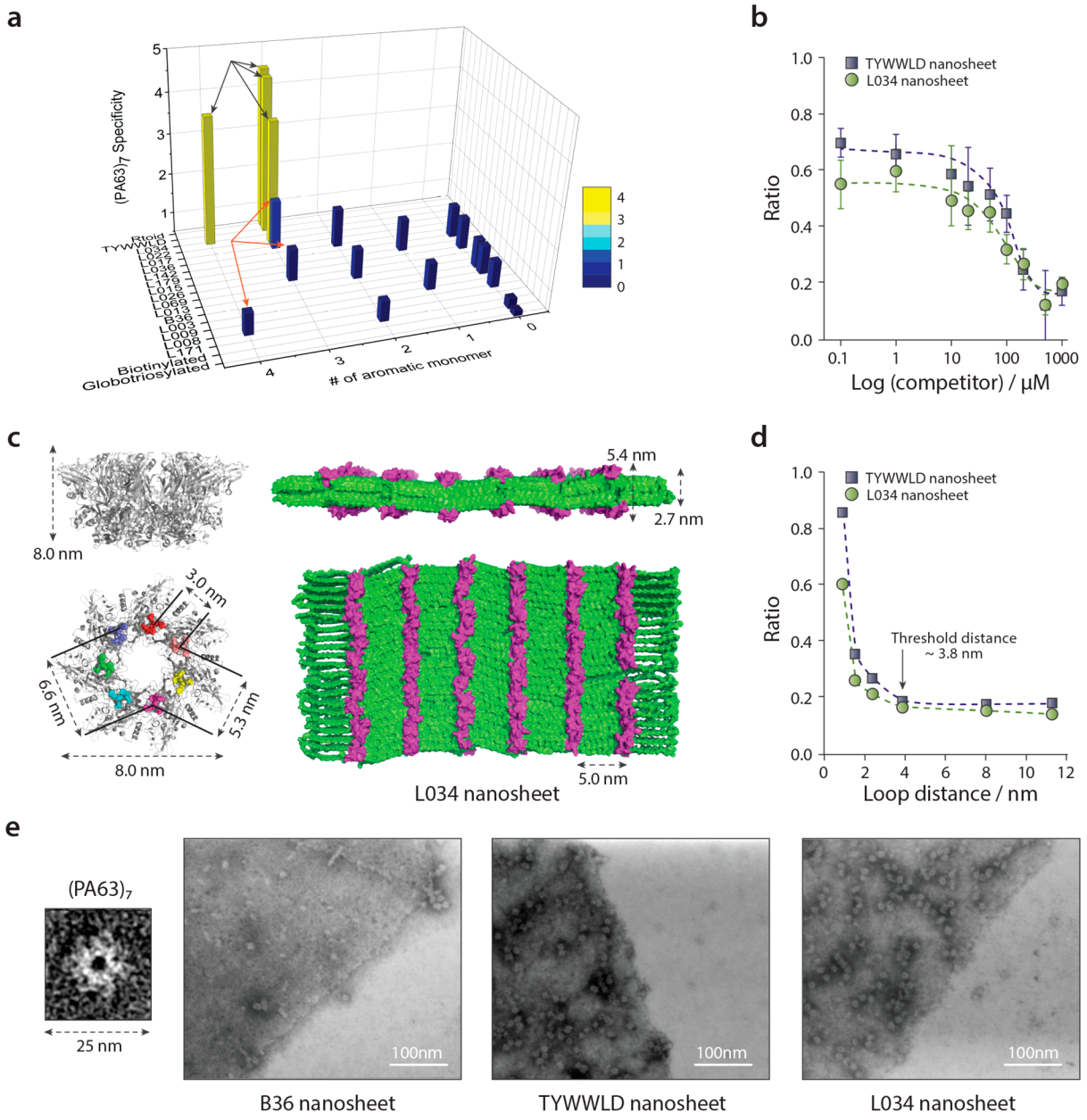

Figure 4. Characterization of selective $(PA63)_7$ binding behavior of L034 nanosheet by monomeric chemical property and multivalent configuration. (a) Relationship of the number of aromatic monomers within loop domain to $(PA63)_7$ specificity score. Arrows indicate loop sequences with aromatic monomers possessing the secondary property as hydrogen bonding donor (black arrows) or others (orange arrows). (b) Competitive binding assay with TYWWLD hexamer as a competitor. (c) Molecular structure of $(PA63)_7$ (PDB 1TZO) and L034 nanosheet. Colored regions in $(PA63)_7$ represent binding site for TYWWLD ligand. L034 nanosheet structure shows the spatial configuration and interspacing of loops (purple) on the backbone chains (green). (d) Degree of $(PA63)_7$ binding as a function of the shortest average loop separation on the nanosheet. (e) Electron microscopic images of B36 (*i.e.*, loopless), TYWWLD and L034 nanosheet with bound $(PA63)_7$.

supramolecular assembly process has been accomplished by the lateral compression of peptoid monolayers formed at the air/water or oil/water interface.[27,28] A device to rotate a glass vial containing milliliter volumes of peptoid-dissolved solutions from vertical to horizontal was designed to induce a 3-fold change of interfacial area for obtaining high-quality peptoid nanosheets. However, the vial-rocking method is too difficult to parallelize for high-throughput library generation and screening and operates at the milliliter scale, which results in an unnecessary waste of material and makes materials cost prohibitively high as the library size increases. To address this challenge, we established a pipetting method for effective preparation of nanosheets that can be performed in multiwell plates with an automated pipetting robot. Withdrawing an aqueous solution by pipetting creates an air/water interface inside the pipet tip. Due to the conical geometry of the tip, the interfacial area changes depending on the volume of liquid aspirated (Figure S1). By repeating aspiration and dispense cycles, surface compression comparable to the vial rocking method could be achieved at much smaller volume scales (~10 μL) (Figure 3a). The quality (size, thickness, and uniformity) of nanosheets synthesized by the pipetting method were in line with that prepared by vial rocking (Figure 3b and Figure S2). Attractive aspects of the pipetting method are that it is readily

DOI: 10.1021/acsnano.9b07498
ACS Nano 2020, 14, 185−195

automated, can be performed in a multiwell plate format, and produces nanosheets at concentrations and in buffers suitable for direct use in subsequent protein-binding screens.

To evaluate the protein-binding capability of each loop-displayed nanosheet, we developed a screening method based on our previously developed homogeneous FRET binding assay.[20] Nanosheet-forming solutions were mixed with octadecyl rhodamine (OR), which anchors its aliphatic tail in the sheet's hydrophobic core, and serves as the FRET donor. These OR-labeled sheets yield a FRET signal upon binding of Alexa Fluor 647 (AF647)-conjugated target proteins on the nanosheet surface (Figure S3). By analyzing fluorescence spectra of control (loopless), biotinylated, and globotriosylated nanosheets in the absence and presence of protein, a positive FRET signal was generated by a binding event of nanosheets to their corresponding targets (Figure S4). Spectral scanning of the surface of the globotriosylated nanosheet by confocal microscopy verified that the FRET signal originated from the protein binding onto the nanosheet surface (Figure S5). To estimate the degree of binding for the selection of hits, the FRET ratio was calculated based on curve fitting to prevent potential errors caused by noise in the fluorescence spectra. We found that this method could satisfactorily identify high-FRET hits similar to the conventional FRET ratio measurements ($\sim I_{Acceptor}/I_{Donor}$) (Figure S6). Analysis of the fitting-corrected ratio for 10 samples of each loopless, biotinylated, and globotriosylated nanosheets in the presence of Shiga toxin 1 subunit B (STX 1B) (Figure S7), revealed a *Z*-factor of approximately 0.73, indicating that this assay is sufficient for high-throughput screening.[29]

We next applied our automated screening platform to discover loop-functionalized nanosheets capable of selective binding to anthrax protective antigen $(PA63)_7$ which is a homoheptameric toxin-related protein. To gauge binding specificity, FRET values of each loopoid nanosheet were obtained against fluorescently labeled $(PA63)_7$ and other multimeric control proteins, STX 1B and streptavidin, and the ratiometric score for binding specificity was calculated. From the parallel screening of a nanosheet library of 60 variants, sample L034 nanosheet was found to have the highest specificity score for $(PA63)_7$ (Figure 3c).

Upon successful identification of a hit for $(PA63)_7$, we scaled up the preparation of several nanosheet candidates to the milliliter scale using the vial-rocking method to allow for more stringent validation and characterization of binding affinity.[28] This seamless transition from microscale screening to macroscale production highlights the utility of this platform for rapid affinity reagent development. After scale-up, we examined the consistency of $(PA63)_7$ binding specificity to the L034 nanosheet by the FRET assay and by fluorescence microscopy. As a positive control, we created a nanosheet that displays a loop containing a known $(PA63)_7$ binding motif composed of a peptide hexamer, TYWWLD, previously discovered by phage-display methods[30,31] (Figure 3d). Fluorescence microscope images and the FRET assay indicate that only $(PA63)_7$ was selectively captured by the L034 nanosheet as well as the specific binding by TYWWLD nanosheet (Figure 3e, Figures S8 and S9). This result demonstrates the ability to rapidly discover antibody mimetics from microscale screening of combinatorial libraries, and immediate scale up of hits to the milligram scale for further testing and use.

Binding Specificity: Chemical Properties and Multivalency of Loop-Functionalized Nanosheets. The $(PA63)_7$ binding hit, L034, has a loop insert sequence of Namd-Ntyr-Ntyr-Ntyr-Ntyr-Namd, which consists of two small polar carboxamidomethyl (Namd) side chains, and four aromatic hydroxyphenethyl (Ntyr) side chains (Figure 3d). Interestingly, this falls into the same **HP** family as the positive control loop (TYWWLD), where there are four central hydrophobic groups flanked by two polar groups (*i.e.*, **PHHHHP**). Additionally, both contain three aromatic residues in the hydrophobic loop region, allowing us to consider the impact of specific chemical features of the loop on $(PA63)_7$ recognition (Table S2). Given the predominance of hydrophobic side chains in both our hit and the positive control sequence, we first examined the binding of other hydrophobic library members. There were five other loop-functionalized nanosheets with the identical **PHHHHP** pattern that did not recognize $(PA63)_7$ (Figure S10) indicating that aromatic richness is the major factor for $(PA63)_7$ recognition. We also explored the importance of multiple aromatic derivatives within the loop domain by designing an all-peptoid analogue (rationally designed peptoid, Rtoid) inspired from the known TYWWLD peptide sequence, which has three aromatic groups (Figure S11). The Rtoid nanosheets exhibited strong binding, indicating that the aromatic side chains are playing a dominant role in binding. Motivated by these observations, we plotted the $(PA63)_7$ specific binding ability against the number of aromatic monomers within the loop region (Figure 4a), which revealed that $\geq$3 aromatic monomers were necessary but insufficient for binding. A secondary chemical property, a hydrogen-bonding donor, is also required for binding. Additional secondary properties such as a hydrogen bonding acceptor or chirality were not required.

The specific binding affinity of loops containing aromatic and hydrogen-bond donor properties hints that they interact with a specific site of $(PA63)_7$. By performing competitive binding experiments of a L034 or TYWWLD nanosheet in the presence of the free TYWWLD hexamer as a competitor (Figure 4b), the half maximal inhibitory concentration (IC_{50}) value of the L034 nanosheet of 78 μM is similar to that of the TYWWLD nanosheet (98 μM), indicating they interact with the same binding site of $(PA63)_7$. A computational docking simulation of the TYWWLD peptide in a loop conformation binding to $(PA63)_7$ provided insight into the molecular interactions involved. The central YWW residues are in close contact ($\leq$4.5 Å) to P184, F202, F203, S204, and P205 which are known to form a hydrophobic binding pocket in $(PA63)_7$.[32] Phenylalanine facilitates an interaction with aromatic peptide residues *via* $\pi-\pi$ interactions. In addition, proline is known to preferentially interact with electron-rich aromatics, such as tyrosine and tryptophan, by CH-π interactions in contrast to electron-poor aromatics and nonaromatics.[33] Taken together, we envisioned that a loop domain comprising many electron-rich aromatic functionalities can recognize the hydrophobic pocket of $(PA63)_7$ *via* $\pi-\pi$ and CH-π interactions.

From a multivalent binding point of view, the spatial arrangement of binding loops on the surface of the peptoid nanosheet plays a key role in its specificity. The distance between loops in the direction of the chain is approximately 5.1 nm, which is close to the second shortest distance, 5.4 nm, between $(PA63)_7$ binding sites, as shown in the simulated structure of the L034 nanosheet (Figure 4c). According to the model, the hydrophobic binding pocket of $(PA63)_7$ covers several loops on the sheet surface, indicating that simultaneous multiple binding events, that is, multivalent binding, may occur. Typically, multivalency leads to nonlinear binding responses

DOI: 10.1021/acsnano.9b07498
ACS Nano 2020, 14, 185−195

such as superselectivity and high binding affinity.[22] We explored the effect of loop display density on $(PA63)_7$ binding by diluting the TYWWLD and L034 loop strands with varying amounts of a loopless nanosheet-forming peptoid. This results in a series of coassembled nanosheets with different interloop spacings. The degree of binding exhibited a nonlinear response versus loop spacing (Figure 4d). The threshold distance of both nanosheets is ~3.8 nm, which is close to the shortest distance between binding sites of $(PA63)_7$. This suggests that the close loop spacing is required for cooperative binding and higher affinity. The multivalent interaction between loops and $(PA63)_7$ was also supported by direct observation *via* transmission electron microscopy which revealed that the central pore of $(PA63)_7$ was vertically aligned on the surface of both the TYWWLD and L034 nanosheets (Figure 4e).

Binding Performance of Loop-Functionalized Nanosheets: Binding Affinity and Proteolytic Stability. To evaluate the feasibility of our identified affinity reagents for practical use, we evaluated their binding performance using biolayer interferometry (BLI) according to our previously developed method.[34] We transferred a loop-functionalized peptoid monolayer onto the hydrophobic surface of the optical fiber by Langmuir–Schaefer deposition, exposing loop domains that can capture target proteins. BLI allows real-time, label-free monitoring of a bound protein based on interference patterns formed by reflection of white light from a functional surface, allowing the measurement of binding affinity. Both L034 and TYWWLD monolayers immediately captured and tightly immobilized $(PA63)_7$ on their surface in accordance with association and dissociation stages. In contrast, there was no binding response with the loopless peptoid monolayer (Figure 5a). Analysis of the binding curves of L034 and TYWWLD revealed that these loop-functionalized monolayers had single-digit nanomolar binding affinity, 2.0 nM and 1.6 nM, respectively, (Table S3), which is comparable to the K_D of recombinant antibodies and natural complementary components (*i.e.*, edema factor and lethal factor) for $(PA63)_7$.[30,35,36] The binding affinity of these materials is strikingly high in comparison with the known micromolar binding of the monovalent TYWWLD ligand.[30] Taken together, these results indicate a significant enhancement of binding affinity due to the high avidity of designed and engineered multimeric structures.[37]

Beyond their exceptional binding performance, these materials hold promise as a robust affinity reagent scaffold due to the chemical stability and durability of peptoids against proteases.[38] To demonstrate this, we monitored the proteolytic stability of the L034 nanosheet by atomic force microscopy. While the all-peptoid L034 nanosheet maintained loop architectures after protease treatment, the initially rough surface of the peptide-containing TYWWLD nanosheet smoothed (Figure 5b). Additionally, the thickness of the L034 nanosheet did not change, whereas the TYWWLD nanosheet thinned from 4.7 to 3.4 nm after protease treatment (Figure 5c). These results indicated that while the peptide loops of the TYWWLD nanosheet were eliminated through proteolytic degradation, the all-peptoid L034 nanosheet has high proteolytic resistance. We further studied the influence of proteolytic degradation on the binding activity of the L034 and TYWWLD nanosheets using multicolor fluorescence imaging, with the Texas Red (TR) filter for nanosheets and the Cy5 filter for the $(PA63)_7$ protein as yellow and red color, respectively (Figure 5d). The orange color of the TYWWLD nanosheet incubated with $(PA63)_7$ turned to yellow after protease treatment, indicating that the removal of

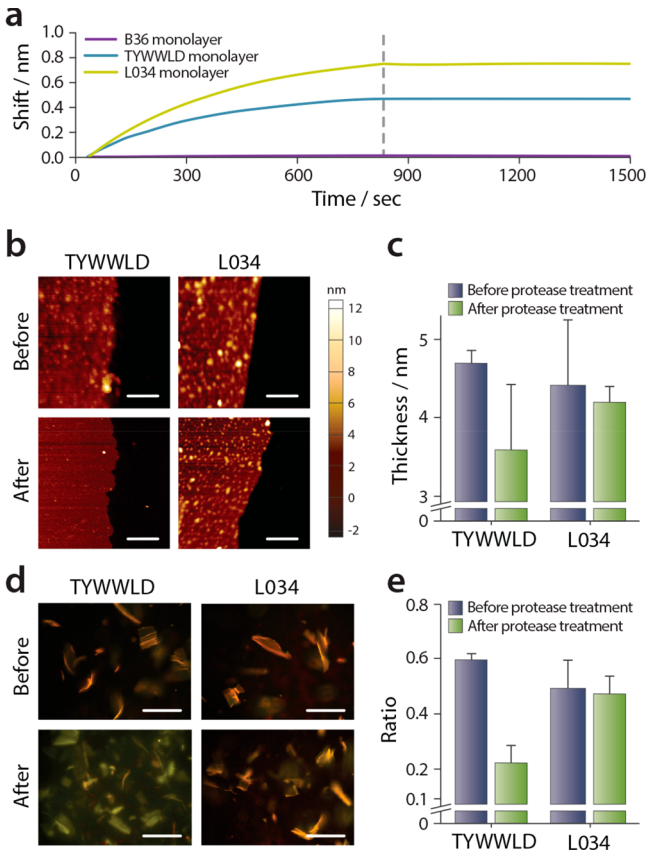

Figure 5. Binding performance and proteolytic stability of L034 nanosheet. (a) Binding response of B36 (*i.e.*, loopless), TYWWLD, and L034 monolayer-deposited optical fiber against $(PA63)_7$ by using the biolayer interferometric technique. Area before and after dotted line represents association and dissociation phase, respectively. (b) AFM images of TYWWLD and L034 nanosheets before and after protease treatment. Scale bars represent 1 μm. (c) Quantification of the thickness upon protease treatment calculated from AFM images. Each thickness was estimated by averaging three AFM measurements. (d) Fluorescence microscopic images of loopoid nanosheets before and after protease treatment. All images were obtained in the presence of $(PA63)_7$ under TR (yellow) and Cy5 (red) filter. Scale bars represent 100 μm. (e) Quantification of the proteolytic stability of TYWWLD and L034 nanosheet by FRET-based assay. L034 nanosheet retains binding affinity after protease treatment, demonstrating resistance to proteolysis.

TYWWLD loops led to the loss of binding affinity to $(PA63)_7$. The L034 nanosheet, however, remained orange in the merged fluorescence image after the incubation of protease, indicating that they retained $(PA63)_7$ binding activity. We corroborated these results with our FRET assay, where proteolytic degradation of TYWWLD loops also demonstrated loss of $(PA63)_7$ binding in contrast to negligible change in FRET signal from the L034 nanosheet (Figure 5e). The durability of these peptoid constructs against proteolysis highlights a major advantage of this synthetic system.

CONCLUSION

We have described an approach to generate 2D antibody mimetic materials with specific protein binding using a purely synthetic approach. The method uses high-throughput screening of combinatorial libraries of non-natural, sequence-defined peptoid polymers folded into protein-like architectures. The selective binding affinity of the L034 nanosheet hit to $(PA63)_7$

DOI: 10.1021/acsnano.9b07498
ACS Nano 2020, 14, 185−195

sensitively depends on the chemical characteristics of the surface-displayed loops. Furthermore, the spatially dense display of surface loops enables high binding avidity that significantly improves binding affinity to the target protein *via* multivalent interactions. This is a major advantage of these non-natural sheets which have a massive binding surface area relative to antibodies, and make them particularly well-suited to engage with large, multivalent targets. Moreover, their non-natural peptoid chemistry makes them robust to proteolytic attack as demonstrated by detailed analysis using AFM, fluorescence imaging, and FRET binding assay. Robustness is a valuable property of using non-natural backbone chemistry, allowing screening in less stringently purified biofluids and discovery of affinity reagents that operate under harsher and more practical use cases. This work advances on several key aspects of antibody mimetic materials, demonstrating a rational and scalable strategy for generating and screening large chemical libraries, generation of materials with high and selective binding affinity *via* multivalency, and the ability to immediately scale up production of hits by simple batch synthesis approaches that do not involve animals. Screening capacity is limited only by the fluidic approach for mixing and testing the combinatorial library members. Using established microfluidic miniaturization approaches, screening hundred-million-member libraries should be feasible, allowing multiple loopoid strands to be combined prior to nanosheet assembly to access enormous chemical diversity akin to the natural immune system. Combined, these properties should allow rapid and effective discovery of robust recognition elements for pathogens (*e.g.*, toxin proteins, viruses, and cells) important to many biomedical applications such as sensing, diagnostics, and therapeutics.

MATERIALS AND METHODS

Instrumentation. Fluorescence data were collected with a BioTek Synergy H1 microplate reader. Fluorescence microscopy was performed on an Olympus IX81 inverted microscope, and confocal FRET experiments were conducted on a Zeiss LSM710 microscope equipped with a spectral detector. Confocal image spectra were collected from images by image thresholding across all channels and background subtraction through ImageJ. Biolayer interferometry measurements were conducted on the Octet Red384 system from ForteBio.

Loopoid Library Synthesis and Purification. Methods for the solid-phase synthesis and purification of peptoid polymers were previously reported by our group and others.[15] Submonomer peptoid synthesis was automated using a Protein Technologies Symphony X or AAPPTEC Apex 396 peptide synthesizers to allow for the parallel synthesis of up to 24 different loopoid sequences at a time. β-Alanine *tert*-butyl ester (Nce) and glycine *tert*-butyl ester (Ncm) were prepared from the HCl salt using 1 M aq NaOH and extracted with DCM before preparation of 1 M solutions in DMF. Glycinamide HCl (Namd) was neutralized in DMF by adding an equimolar amount of KOH (50% w/w aq solution) and filtered by centrifugation immediately before use. Protected ethanolamine (Nhe) was prepared according to published procedures.[39] All other amines were purchased from commercial suppliers and used without further purification. Peptoid loopoids were prepared using a Rink amide resin (200 mg) from Protein Technologies with a standard amine loading of 0.64 mmol/g. Standard peptoid coupling proceeded in two steps, initial bromoacetylation with bromoacetic acid (BrAA, 0.8 M) and *N*,*N*-diisopropylcarbodiimide (DIC, 0.8 M) in *N*,*N*-dimethylformamide (DMF) for 2.5 min. Subsequent displacement with amine (1 M) in DMF lasted for 5 min. Anilines, and other low nucleophilicity amines, were bromoacetylated for 20 min and their displacement lasted for 1 h using amine (2 M) solutions with added potassium iodide (1 M).[40]

The TYWWLD loopoid strand was prepared on a low loading (200 mg, 0.2 mmol/g) Rink amide resin from Protein Technologies to counter aggregation. Peptoid coupling proceeded with the standard reagents using 1 h displacement and bromoacetylation times. Amino acids in the loop were coupled twice with HCTU (0.4 M), *N*-methylmorpholine (0.4 M), and Fmoc-protected amino acids (0.4 M) in DMF for 1 h and then deprotected with 4-methylpiperidine (20% v/v) for 1 h. The TYWWLD hexamer was prepared on standard Rink amide resin using DIC (0.8 M) as coupling agent with 1 h coupling and deprotection times.

Crude loopoids were cleaved from the resin using 95% TFA/2.5% H_2O/2.5% TIPS while mixing on a rotary shaker for 30 min. The cleaved peptoid was filtered and resin was washed with DCM before concentration of the combined organics on a Biotage V10 evaporator. The loopoids were purified by reverse-phase HPLC using a Waters XBridge Prep C18 (5 μm, 19 × 100 mm) column. The typical gradient was 35−65% over 30 min with H_2O+0.1% TFA as solvent A and ACN +0.1% TFA as solvent B. The pure fractions were combined and concentrated with a Biotage V10 evaporator before dissolving with Milli-Q water and lyophilizing to produce a typical yield of 15−30 mg. Purified loopoids were evaluated by analytical reverse-phase HPLC and MALDI-TOF mass spec to meet a standard of ≥85% purity for inclusion in the library screening.

Loop-Functionalized Nanosheet Assembly and Screening. A library of loopoid nanosheets was prepared with a robotic liquid handling system (Biomek FX, Beckman Coulter) as follows. Each well of 96-well plates (polypropylene, round-bottom; Greiner Bio-One, cat. no. 655209) was filled with 247.5 μL of 5 μM OR (octadecyl rhodamine B chloride; ThermoFisher, cat. no. O246) in 10 mM Tris buffer (pH 8.0). 2.5 μL of 2 mM loopoid stock solution in 2:1 (v/v) DMSO/water was added to each well to make a final loopoid concentration of 20 μM. The robotic pipettor with a 96-channel head (AP96) was programmed to perform 3:1 interfacial area compression inside a P250 pipet tip as follows (Figure S1; Beckman Coulter, cat. no. 717252): (a) aspirate 200 μL of loopoid solution; (b) 200 cycles of dispense 160 at 16 μL/s flow rate, aspirate 160 at 32 μL/s with a delay time of 10 s after the aspiration; (c) dispense 200 μL. Then, 50 μL of nanosheet-containing solutions were transferred to the plates prefilled with 50 μL of Alexa 647-conjugated substrate protein solutions and mixed with the 96-channel pipet head. After 30 min incubation at room temperature, the fluorescence intensities and/or spectra of both donor and acceptor fluorophores were obtained with a plate reader (Infinite M200 PRO, Tecan; excitation at 550 nm, donor emission at 590 nm, isosbestic point at 645 nm, acceptor emission at 675 nm) and analyzed to calculate FRET ratios. Fluorescence images of produced nanosheets were acquired with an automated microscope (EVOS FL Auto, Life Technologies) using the RFP light cube (Ex. 531/40 nm, Em. 593/40 nm) with a raster scan mode, and the images from the same well were stitched together with the manufacturer provided software (PerlScope, revision no. 31201).

To compare binding specificity quantitatively, we calculate specificity score (S) for each loopoid (i = 1, 2, ⋯, n) and each target protein (j = 1, 2, ⋯, m) from FRET ratio values (R_{ij}) as follows: (1) filter out loopoids with negative FRET ratio values due to background noise ($R_{ij} > 0$); (2) normalize FRET ratio values for each target protein group by dividing the values with the maximum FRET value from each group ($R'_{ij} = \frac{R_{ij}}{\max_i(R_{ij})}$); (3) calculate the relative ratio as defined:

$$S_{ik} = \frac{(m-1)R'_{ik}}{\sum_{j\neq k} R'_{ij}}$$

For example, when FRET ratio values for three target proteins (anthrax, shiga, and strep) are available from a binding affinity screen, the anthrax binding specificity score for loopoid i is calculated as

$$S_{i,\mathrm{anth}} = \frac{R'_{i,\mathrm{anth}}}{(R'_{i,\mathrm{shiga}} + R'_{i,\mathrm{strep}})/2}$$

For hit validation, nanosheets were prepared by the conventional vial-rocking method according to the literature.[28] Briefly, 1 mL of Tris

DOI: 10.1021/acsnano.9b07498
ACS Nano 2020, 14, 185−195

buffer (10 mM, pH 8.0) containing 20 μM peptoid strands were prepared in a 4 dram glass vial. The vial was tilted by a custom-built machine from horizontal to vertical for 200 repetitions and 10 s horizontal wait times.

$(PA63)_7$ Expression, Purification, and Dye Labeling. A plasmid for expression of the 83 kDa anthrax protective antigen (PA83; K563C, D425A mutant) cloned into a pD444-ompA vector (ATUM, Newark, CA) with ampicillin resistance, IPTG inducible T5 promoter and ompA signal peptide was a gift from the Pentelute lab at MIT. Similar protocols for purification of $(PA63)_7$ have been described previously.[41,42] BL21 (DE3) *Escherichia coli* (New England Biosciences, Ipswich, MA) transformants were grown from overnight cultures in 0.5 L batches at 37 °C with shaking at 250 rpm to OD 0.6–0.8. Overexpression was induced with 1 mM IPTG at 30 °C and 250 rpm for 3 h. Cells were harvested by centrifugation and stored as pellets at −80 °C until protein purification. Cells were exposed to osmotic shock to extract proteins from the periplasmic space by dispersion in 10 mM bis-tris propane pH 8.9 with 1 mM EDTA and 30% glucose, followed by centrifugation and redispersion into 5 mM $MgCl_2$. A round of ultracentrifugation was used to clarify the supernatant (50 000*g*, 30 min), then the solution was brought to 10 mM bis-tris propane pH 8.9 with 5 mM TCEP (Buffer A) with concentrated stocks. This solution was applied to a 5 mL HiTrap Q Fast Flow anion exchange column (GE Healthcare Life Sciences, Marlborough, MA) and eluted over 20 column volumes with a 0–60% gradient of Buffer A + 1 M NaCl. The fraction containing PA83 was identified by SDS-PAGE and dialyzed into Buffer A overnight at 4 °C. Cleavage of PA83 to the active PA63 form was done by adding 1:1000 (g/g) trypsin/PA63 for 30 min at room temperature, followed by the addition of a 10 times excess of trypsin inhibitor. It was found that heptamerization of PA63 did not occur until a second round of anion exchange (this time over a 1 mL column) after cleavage to separate PA63 from the 20 kDa cleaved unit. The $(PA63)_7$-containing fraction was dialyzed into phosphate buffered saline pH 7.4 (PBS; 10 mM phosphate buffer, 2.7 mM potassium chloride, and 137 mM sodium chloride) overnight at 4 °C.

Alexa Fluor 647 succinimidyl ester (ThermoFisher Scientific, Waltham, MA) was conjugated to solvent-exposed lysine residues of $(PA63)_7$. The protein in PBS pH 7.4 solution was made basic with 1 M sodium bicarbonate pH 9.0, and dye was dissolved in dry DMSO. Ten molar equivalents of the dye (relative to heptamer concentration obtained by UV–vis absorbance at 280 nm using a measured extinction coefficient of 4.39×10^5 M^{-1} cm^{-1}) was added to the protein solution while stirring vigorously, and the reaction was allowed to proceed for 1 h. The reaction was quenched with 0.2 M tris(hydroxymethyl)-aminomethane hydrochloride pH 7.5 and the protein was purified as a heptamer *via* gel filtration with a Superdex 200 Increase 10/300 GL column (GE Healthcare Life Sciences, Marlborough, MA). Final protein concentrations were measured by UV–vis, and samples were stored in PBS pH 7.4 at 4 °C.

Scanning Transmission Electron Microscope Sample Preparation. Nanosheet samples were combined 1:1 with 1 mM $(PA63)_7$ in PBS pH 7.4. The solution was drop-cast onto copper TEM grids (ultrathin carbon with lacey carbon film, 400 mesh, Ted Pella, Redding, CA) and allowed to incubate for 10 min. After wicking away the sample solution and washing twice with water, an organotungsten negative stain (Nano-W, Nanoprobes, Yaphank, NY) was applied for 5 min. The stain was wicked away and the samples were allowed to air-dry overnight before imaging at 30 kV in STEM mode on a Zeiss Gemini Ultra-55 analytical FE-SEM.

Transmission Electron Microscope Sample Preparation. Negative staining EM specimen preparation: PA63 Heptamer sample was prepared by optimized negative staining method as described.[43−45] In brief, the sample was diluted to 0.01 mg/mL with Dulbecco's phosphate buffered saline (DPBS). An aliquot (~4 μL) of sample was placed on a glow-discharged thin-carbon-coated 200 mesh copper grid (CF200-Cu-UL, Electron Microscopy Sciences, Hatfield, PA 19440, USA). After ~1 min incubation, excess solution was blotted with filter paper. Then, the grid was stained by 1% (w/v) uranyl formate (UF) on Parafilm. The grid was dried with nitrogen.

EM Data Acquisition and Image Processing. The negative staining EM specimen was examined on a Zeiss Libra 120 Plus TEM (Carl Zeiss NTS, Oberkochen, Germany) operating at 120 kV with 20 eV in-column energy filtering at room temperature. The micrographs were acquired by a Gatan UltraScan 4Kx4K CCD at 80 000× magnification (each pixel of the micrographs corresponded to 1.48 Å) under near Scherzer focus (0.1 μm) and defocus of 0.4 μm.

Protease Treatment of Peptoid Nanosheets. For the observation of the proteolytic stability of a loop-functionalized nanosheet, a fresh stock solution of 20 mg/mL proteinase K, 4 mM $CaCl_2$ was prepared in DI H_2O. A 500 mL nanosheet solution was incubated with proteinase K at 60 °C, and agitated on a rotary shaker at 300 rpm overnight. Final concentration is 0.25 mg/mL of Proteinase K, 4 mM $CaCl_2$, and 50 mM Tris pH 7.5 buffer. After incubation with Proteinase K, nanosheets were dialyzed overnight, using a 1 mL Spectra-Por Float-A-Lyzer device with 100 kDa MWCO to remove Proteinase K. The dialyzed samples were transferred onto the surface of freshly cleaved mica to observe morphology by AFM.

ASSOCIATED CONTENT

Supporting Information

The Supporting Information is available free of charge at https://pubs.acs.org/doi/10.1021/acsnano.9b07498.

Design and synthesis of the peptoid library, microscale formation of nanosheet libraries, nanosheet characterization, FRET assay validation and binding data, analysis of binding specificity (PDF)

AUTHOR INFORMATION

Corresponding Authors

*E-mail: arabate@gmail.com.
*E-mail: rnzuckermann@lbl.gov.

ORCID

Samuel C. Kim: 0000-0001-5237-6358
Tengyue Jian: 0000-0002-4463-5492
Lisa Yun: 0000-0001-7940-4902
Gang Ren: 0000-0002-8036-2321
Chun-Long Chen: 0000-0002-5584-824X
Adam R. Abate: 0000-0001-9614-4831
Ronald N. Zuckermann: 0000-0002-3055-8860

Author Contributions

#J.H.K. and S.C.K. contributed equally to this work. R.N.Z., A.R.A., K.K., and C.L.C. conceived the project and directed the work. M.A.K., B.W.T., D.C.D., Y.C., V.U., T.J., and M.D.C. performed the synthesis and purification of the peptoid polymers. J.H.K., S.C.K., J.C., and M.K. produced the nanosheet libraries for screening. J.H.K., S.C.K., and E.M.G. developed the screening method and performed the screening assays. D.J.M. developed the sensor-coating method. L.Y. and J.C. characterized the nanosheets produced for screening. J.L. and G.R. performed electron microscopy of the nanosheets binding to target proteins. J.H.K., S.C.K., A.R.A., and R.N.Z. wrote the manuscript with input from others.

Notes

The authors declare no competing financial interest.

ACKNOWLEDGMENTS

This project was funded by the DARPA Fold F(x) program. Portions of this work were conducted at the Molecular Foundry at Lawrence Berkeley National Laboratory, which is supported by the Office of Science, Office of Basic Energy Sciences, U.S. Department of Energy under Contract No. DEAC02-05CH11231. Pacific Northwest National Laboratory (PNNL)

DOI: 10.1021/acsnano.9b07498
ACS Nano 2020, 14, 185−195

is a multiprogram national laboratory operated for Department of Energy by Battelle under Contracts No. DE-AC05-76RL01830. The authors thank R. Garcia for help with peptoid synthesis.

REFERENCES

(1) Bradbury, A. R.; Sidhu, S.; Dubel, S.; McCafferty, J. Beyond Natural Antibodies: The Power of *In Vitro* Display Technologies. *Nat. Biotechnol.* **2011**, *29*, 245−254.
(2) Holliger, P.; Hudson, P. J. Engineered Antibody Fragments and the Rise of Single Domains. *Nat. Biotechnol.* **2005**, *23*, 1126−1136.
(3) Haussner, C.; Lach, J.; Eichler, J. Synthetic Antibody Mimics for the Inhibition of Protein-Ligand Interactions. *Curr. Opin. Chem. Biol.* **2017**, *40*, 72−77.
(4) Binz, H. K.; Amstutz, P.; Pluckthun, A. Engineering Novel Binding Proteins from Nonimmunoglobulin Domains. *Nat. Biotechnol.* **2005**, *23*, 1257−1268.
(5) Mahon, C. S.; Fulton, D. A. Mimicking Nature with Synthetic Macromolecules Capable of Recognition. *Nat. Chem.* **2014**, *6*, 665−672.
(6) Kodadek, T. Synthetic Receptors with Antibody-Like Binding Affinities. *Curr. Opin. Chem. Biol.* **2010**, *14*, 713−720.
(7) Elgersma, R. C.; Mulder, G. E.; Kruijtzer, J. A. W.; Posthuma, G.; Rijkers, D. T. S.; Liskamp, R. M. J. Transformation of the Amyloidogenic Peptide Amylin(20−29) into Its Corresponding Peptoid and Retropeptoid: Access to Both an Amyloid Inhibitor and Template for Self-Assembled Supramolecular Tapes. *Bioorg. Med. Chem. Lett.* **2007**, *17*, 1837−1842.
(8) Murnen, H. K.; Rosales, A. M.; Jaworski, J. N.; Segalman, R. A.; Zuckermann, R. N. Hierarchical Self-Assembly of a Biomimetic Diblock Copolypeptoid into Homochiral Superhelices. *J. Am. Chem. Soc.* **2010**, *132*, 16112−16119.
(9) Nam, K. T.; Shelby, S. A.; Choi, P. H.; Marciel, A. B.; Chen, R.; Tan, L.; Chu, T. K.; Mesch, R. A.; Lee, B. C.; Connolly, M. D.; Kisielowski, C.; Zuckermann, R. N. Free-Floating Ultrathin Two-Dimensional Crystals from Sequence-Specific Peptoid Polymers. *Nat. Mater.* **2010**, *9*, 454−460.
(10) Hebert, M. L.; Shah, D. S.; Blake, P.; Turner, J. P.; Servoss, S. L. Tunable Peptoid Microspheres: Effects of Side Chain Chemistry and Sequence. *Org. Biomol. Chem.* **2013**, *11*, 4459−4464.
(11) Sun, J.; Jiang, X.; Lund, R.; Downing, K. H.; Balsara, N. P.; Zuckermann, R. N. Self-Assembly of Crystalline Nanotubes from Monodisperse Amphiphilic Diblock Copolypeptoid Tiles. *Proc. Natl. Acad. Sci. U. S. A.* **2016**, *113*, 3954−3959.
(12) Jin, H.; Ding, Y.-H.; Wang, M.; Song, Y.; Liao, Z.; Newcomb, C. J.; Wu, X.; Tang, X.-Q.; Li, Z.; Lin, Y.; Yan, F.; Jian, T.; Mu, P.; Chen, C.-L. Designable and Dynamic Single-Walled Stiff Nanotubes Assembled from Sequence-Defined Peptoids. *Nat. Commun.* **2018**, *9*, 270.
(13) Jin, H.; Jiao, F.; Daily, M. D.; Chen, Y.; Yan, F.; Ding, Y.-H.; Zhang, X.; Robertson, E. J.; Baer, M. D.; Chen, C.-L. Highly Stable and Self-Repairing Membrane-Mimetic 2D Nanomaterials Assembled from Lipid-Like Peptoids. *Nat. Commun.* **2016**, *7*, 12252.
(14) Xuan, S.; Jiang, X.; Spencer, R. K.; Li, N. K.; Prendergast, D.; Balsara, N. P.; Zuckermann, R. N. Atomic-Level Engineering and Imaging of Polypeptoid Crystal Lattices. *Proc. Natl. Acad. Sci. U. S. A.* **2019**, *116*, 22491−22499.
(15) Zuckermann, R. N.; Kerr, J. M.; Kent, S. B. H.; Moos, W. H. Efficient Method for the Preparation of Peptoids [Oligo(*N*-Substituted Glycines)] by Submonomer Solid-Phase Synthesis. *J. Am. Chem. Soc.* **1992**, *114*, 10646−10647.
(16) Knight, A. S.; Zhou, E. Y.; Francis, M. B.; Zuckermann, R. N. Sequence Programmable Peptoid Polymers for Diverse Materials Applications. *Adv. Mater.* **2015**, *27*, 5665−5691.
(17) Robertson, E. J.; Battigelli, A.; Proulx, C.; Mannige, R. V.; Haxton, T. K.; Yun, L.; Whitelam, S.; Zuckermann, R. N. Design, Synthesis, Assembly, and Engineering of Peptoid Nanosheets. *Acc. Chem. Res.* **2016**, *49*, 379−389.
(18) Olivier, G. K.; Cho, A.; Sanii, B.; Connolly, M. D.; Tran, H.; Zuckermann, R. N. Antibody-Mimetic Peptoid Nanosheets for Molecular Recognition. *ACS Nano* **2013**, *7*, 9276−9286.
(19) Zhu, L.; Zhao, Z.; Cheng, P.; He, Z.; Cheng, Z.; Peng, J.; Wang, H.; Wang, C.; Yang, Y.; Hu, Z. Antibody-Mimetic Peptoid Nanosheet for Label-Free Serum-Based Diagnosis of Alzheimer's Disease. *Adv. Mater.* **2017**, *29*, 1700057.
(20) Battigelli, A.; Kim, J. H.; Dehigaspitiya, D. C.; Proulx, C.; Robertson, E. J.; Murray, D. J.; Rad, B.; Kirshenbaum, K.; Zuckermann, R. N. Glycosylated Peptoid Nanosheets as a Multivalent Scaffold for Protein Recognition. *ACS Nano* **2018**, *12*, 2455−2465.
(21) Jiang, S. Y.; Cao, Z. Q. Ultralow-Fouling, Functionalizable, and Hydrolyzable Zwitterionic Materials and Their Derivatives for Biological Applications. *Adv. Mater.* **2010**, *22*, 920−932.
(22) Martinez-Veracoechea, F. J.; Frenkel, D. Designing Super Selectivity in Multivalent Nano-Particle Binding. *Proc. Natl. Acad. Sci. U. S. A.* **2011**, *108*, 10963−10968.
(23) Sun, J.; Zuckermann, R. N. Peptoid Polymers: A Highly Designable Bioinspired Material. *ACS Nano* **2013**, *7*, 4715−4732.
(24) Miller, S. M.; Simon, R. J.; Ng, S.; Zuckermann, R. N.; Kerr, J. M.; Moos, W. H. Comparison of the Proteolytic Susceptibilities of Homologous L-Amino Acid, D-Amino Acid, and N-Substituted Glycine Peptide and Peptoid Oligomers. *Drug Dev. Res.* **1995**, *35*, 20−32.
(25) Flood, D.; Proulx, C.; Robertson, E. J.; Battigelli, A.; Wang, S.; Schwartzberg, A. M.; Zuckermann, R. N. Improved Chemical and Mechanical Stability of Peptoid Nanosheets by Photo-Crosslinking the Hydrophobic Core. *Chem. Commun.* **2016**, *52*, 4753−4756.
(26) Shin, S. B. Y.; Yoo, B.; Todaro, L. J.; Kirshenbaum, K. Cyclic Peptoids. *J. Am. Chem. Soc.* **2007**, *129*, 3218−3225.
(27) Robertson, E. J.; Olivier, G. K.; Qian, M.; Proulx, C.; Zuckermann, R. N.; Richmond, G. L. Assembly and Molecular Order of Two-Dimensional Peptoid Nanosheets through the Oil-Water Interface. *Proc. Natl. Acad. Sci. U. S. A.* **2014**, *111*, 13284−13289.
(28) Sanii, B.; Kudirka, R.; Cho, A.; Venkateswaran, N.; Olivier, G. K.; Olson, A. M.; Tran, H.; Harada, R. M.; Tan, L.; Zuckermann, R. N. Shaken, Not Stirred: Collapsing a Peptoid Monolayer to Produce Free-Floating, Stable Nanosheets. *J. Am. Chem. Soc.* **2011**, *133*, 20808−20815.
(29) Zhang, J. H.; Chung, T. D. Y.; Oldenburg, K. R. A Simple Statistical Parameter for Use in Evaluation and Validation of High Throughput Screening Assays. *J. Biomol. Screening* **1999**, *4*, 67−73.
(30) Mourez, M.; Kane, R. S.; Mogridge, J.; Metallo, S.; Deschatelets, P.; Sellman, B. R.; Whitesides, G. M.; Collier, R. J. Designing a Polyvalent Inhibitor of Anthrax Toxin. *Nat. Biotechnol.* **2001**, *19*, 958−961.
(31) Patke, S.; Boggara, M.; Maheshwari, R.; Srivastava, S. K.; Arha, M.; Douaisi, M.; Martin, J. T.; Harvey, I. B.; Brier, M.; Rosen, T.; Mogridge, J.; Kane, R. S. Design of Monodisperse and Well-Defined Polypeptide-Based Polyvalent Inhibitors of Anthrax Toxin. *Angew. Chem., Int. Ed.* **2014**, *53*, 8037−8040.
(32) Joshi, A.; Kate, S.; Poon, V.; Mondal, D.; Boggara, M. B.; Saraph, A.; Martin, J. T.; McAlpine, R.; Day, R.; Garcia, A. E.; Mogridge, J.; Kane, R. S. Structure-Based Design of a Heptavalent Anthrax Toxin Inhibitor. *Biomacromolecules* **2011**, *12*, 791−796.
(33) Zondlo, N. J. Aromatic-Proline Interactions: Electronically Tunable CH/π Interactions. *Acc. Chem. Res.* **2013**, *46*, 1039−1049.
(34) Murray, D. J.; Kim, J. H.; Grzincic, E. M.; Kim, S. C.; Abate, A. R.; Zuckermann, R. N. Uniform, Large-Area, Highly Ordered Peptoid Monolayer and Bilayer Films for Sensing Applications. *Langmuir* **2019**, *35*, 13671−13680.
(35) Maynard, J. A.; Maassen, C. B.; Leppla, S. H.; Brasky, K.; Patterson, J. L.; Iverson, B. L.; Georgiou, G. Protection against Anthrax Toxin by Recombinant Antibody Fragments Correlates with Antigen Affinity. *Nat. Biotechnol.* **2002**, *20*, 597−601.
(36) Mohamed, N.; Clagett, M.; Li, J.; Jones, S.; Pincus, S.; D'Alia, G.; Nardone, L.; Babin, M.; Spitalny, G.; Casey, L. A High-Affinity Monoclonal Antibody to Anthrax Protective Antigen Passively Protects

DOI: 10.1021/acsnano.9b07498
ACS Nano 2020, 14, 185−195

Rabbits before and after Aerosolized *Bacillus Anthracis* Spore Challenge. *Infect. Immun.* **2005**, *73*, 795−802.
(37) Strauch, E. M.; Bernard, S. M.; La, D.; Bohn, A. J.; Lee, P. S.; Anderson, C. E.; Nieusma, T.; Holstein, C. A.; Garcia, N. K.; Hooper, K. A.; Ravichandran, R.; Nelson, J. W.; Sheffler, W.; Bloom, J. D.; Lee, K. K.; Ward, A. B.; Yager, P.; Fuller, D. H.; Wilson, I. A.; Baker, D. Computational Design of Trimeric Influenza-Neutralizing Proteins Targeting the Hemagglutinin Receptor Binding Site. *Nat. Biotechnol.* **2017**, *35*, 667−671.
(38) Miller, S. M.; Simon, R. J.; Ng, S.; Zuckermann, R. N.; Kerr, J. M.; Moos, W. H. Proteolytic Studies of Homologous Peptide and *N*-Substituted Glycine Peptoid Oligomers. *Bioorg. Med. Chem. Lett.* **1994**, *4*, 2657−2662.
(39) Zuckermann, R. N.; Martin, E. J.; Spellmeyer, D. C.; Stauber, G. B.; Shoemaker, K. R.; Kerr, J. M.; Figliozzi, G. M.; Goff, D. A.; Siani, M. A.; Simon, R. J.; Banville, S. C.; Brown, E. G.; Wang, L.; Richter, L. S.; Moos, W. H. Discovery of Nanomolar Ligands for 7-Transmembrane G-Protein-Coupled Receptors from a Diverse *N*-(Substituted)Glycine Peptoid Library. *J. Med. Chem.* **1994**, *37*, 2678−2685.
(40) Proulx, C.; Yoo, S.; Connolly, M. D.; Zuckermann, R. N. Accelerated Submonomer Solid-Phase Synthesis of Peptoids Incorporating Multiple Substituted *N*-Aryl Glycine Monomers. *J. Org. Chem.* **2015**, *80*, 10490−10497.
(41) Wigelsworth, D. J.; Krantz, B. A.; Christensen, K. A.; Lacy, D. B.; Juris, S. J.; Collier, R. J. Binding Stoichiometry and Kinetics of the Interaction of a Human Anthrax Toxin Receptor, Cmg2, with Protective Antigen. *J. Biol. Chem.* **2004**, *279*, 23349−23356.
(42) Christensen, K. A.; Krantz, B. A.; Collier, R. J. Assembly and Disassembly Kinetics of Anthrax Toxin Complexes. *Biochemistry* **2006**, *45*, 2380−2386.
(43) Zhang, L.; Song, J.; Newhouse, Y.; Zhang, S.; Weisgraber, K. H.; Ren, G. An Optimized Negative-Staining Protocol of Electron Microscopy for Apoe4 Popc Lipoprotein. *J. Lipid Res.* **2010**, *51*, 1228−1236.
(44) Rames, M.; Yu, Y.; Ren, G. Optimized Negative Staining: A High-Throughput Protocol for Examining Small and Asymmetric Protein Structure by Electron Microscopy. *J. Visualized Exp.* **2014**, No. e51087.
(45) Zhang, L.; Song, J.; Cavigiolio, G.; Ishida, B. Y.; Zhang, S.; Kane, J. P.; Weisgraber, K. H.; Oda, M. N.; Rye, K. A.; Pownall, H. J.; Ren, G. Morphology and Structure of Lipoproteins Revealed by an Optimized Negative-Staining Protocol of Electron Microscopy. *J. Lipid Res.* **2011**, *52*, 175−184.

DOI: 10.1021/acsnano.9b07498
ACS Nano 2020, 14, 185−195

Supplementary Information

Discovery of Stable and Selective Antibody Mimetics from Combinatorial Libraries of Polyvalent, Loop-Functionalized Peptoid Nanosheets

Jae Hong Kim,[†1] Samuel C. Kim, [†2] Mark A. Kline,[1] Elissa M. Grzincic,[1] Blakely W. Tresca,[1] Joshua Cardiel,[2] Mohsen Karbaschi,[2] Dilani C. Dehigaspitiya,[3] Yulin Chen,[4] Venkatareddy Udumula,[4] Tengyue Jian,[4] Daniel J. Murray,[1] Lisa Yun,[1] Michael D. Connolly[1], Jianfang Liu,[1] Gang Ren,[1] Chun-Long Chen,[4] Kent Kirshenbaum,[3] Adam R. Abate*,[2, 5] Ronald N. Zuckermann*[1]

[1]The Molecular Foundry, Lawrence Berkeley National Laboratory, 1 Cyclotron Road, Berkeley, CA 94720, USA.

[2]Department of Bioengineering and Therapeutic Sciences, University of California, San Francisco, 1700 4th street, San Francisco, CA 94158 USA.

[3]Department of Chemistry, New York University, 100 Washington Square East, New York, NY 10003, USA.

[4]Physical Sciences Division, Pacific Northwest National Laboratory, Richland, WA 99352, USA.

[5]Chan Zuckerberg Biohub, San Francisco, CA 94158, USA.

Table of Contents

A. LOOPOID LIBRARY

Characterization of free peptoids by analytical HPLC and MALDI-TOF

Several representative peptoid strands are shown in this section.

TYWWLD-inserted loopoid strand

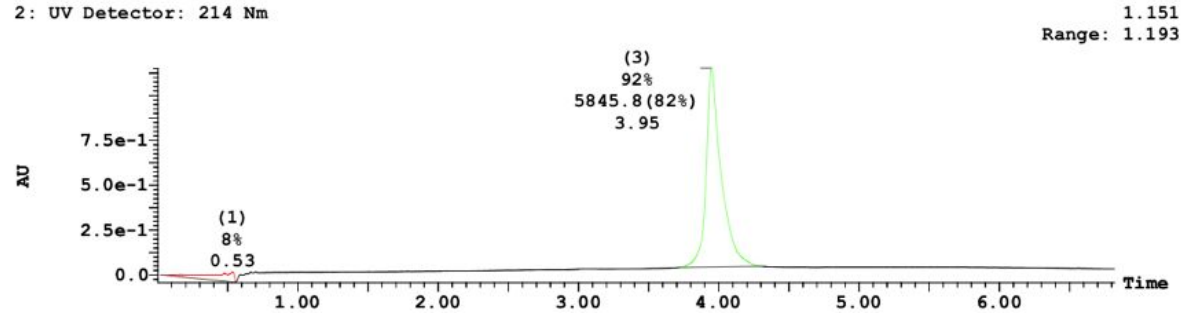

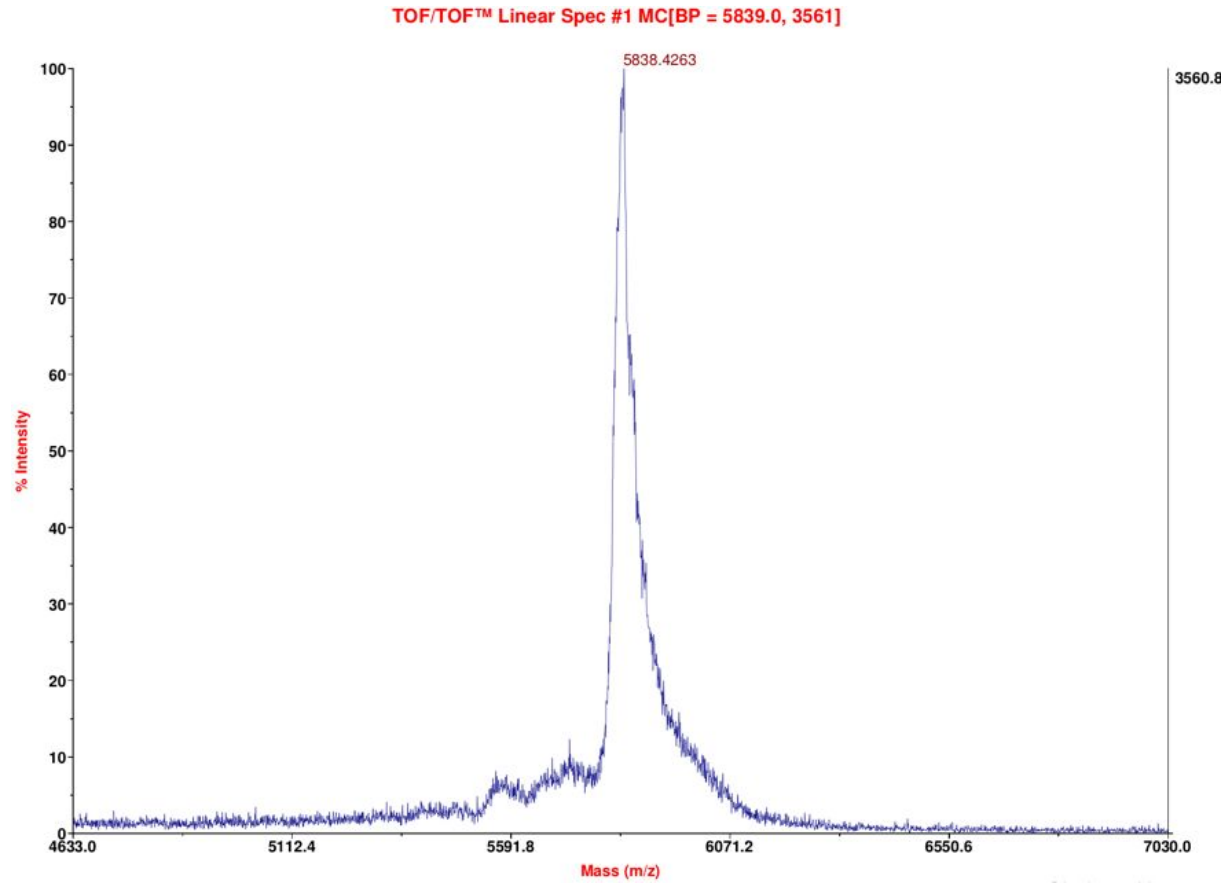

UPLC (5-95% 6.8 min) RT = 3.95 min.
MALDI-TOF calc. $(M+H)^+$ = 5847.78, obs. = 5838.43

TYWWLD-inspired loopoid strand (Rtoid)

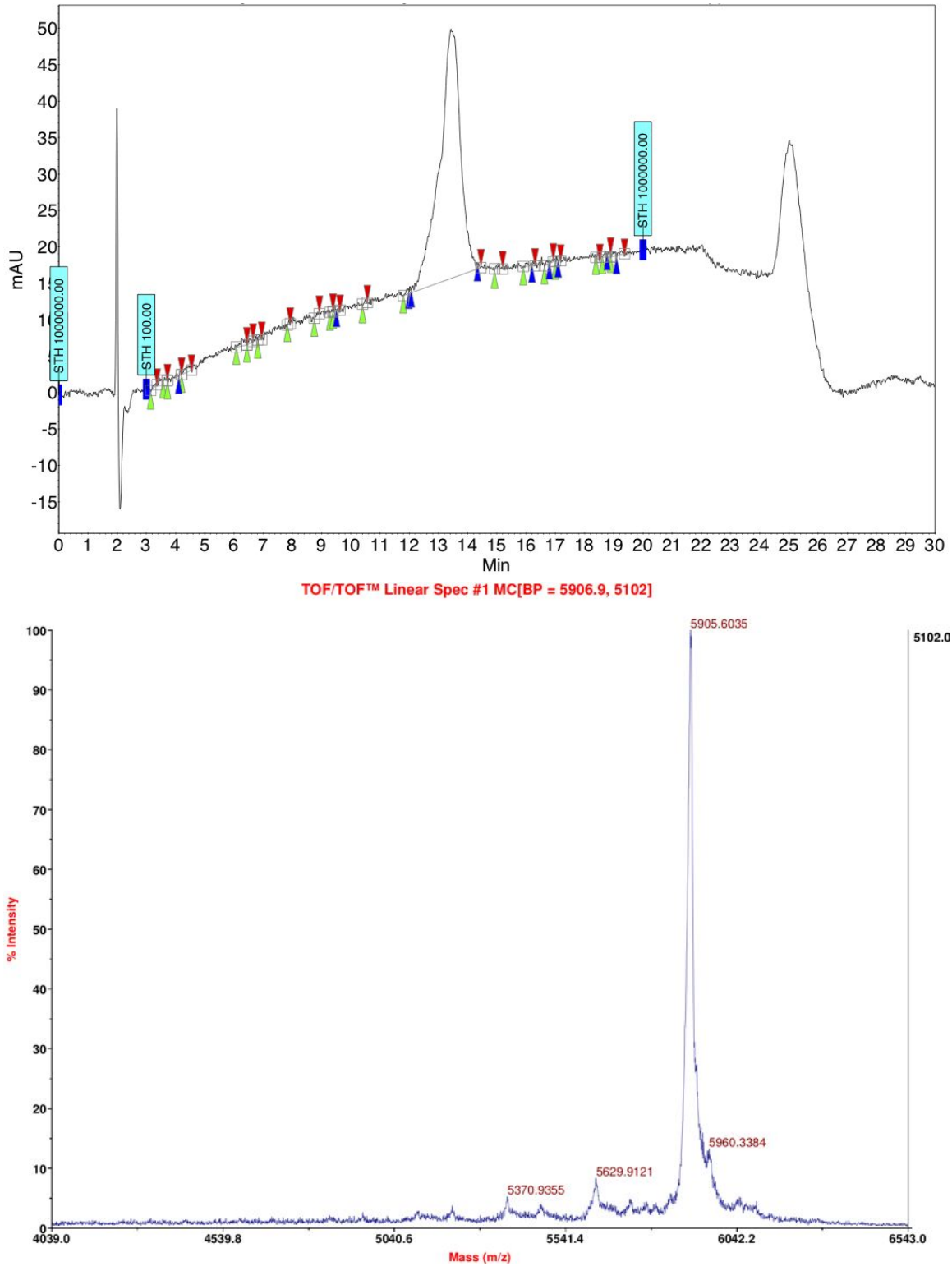

HPLC (5-95% 20 min) RT = 13.44 min

MALDI-TOF calc. $(M+H)^+$ = 5917.92, obs. = 5905.60

L002 loopoid strand

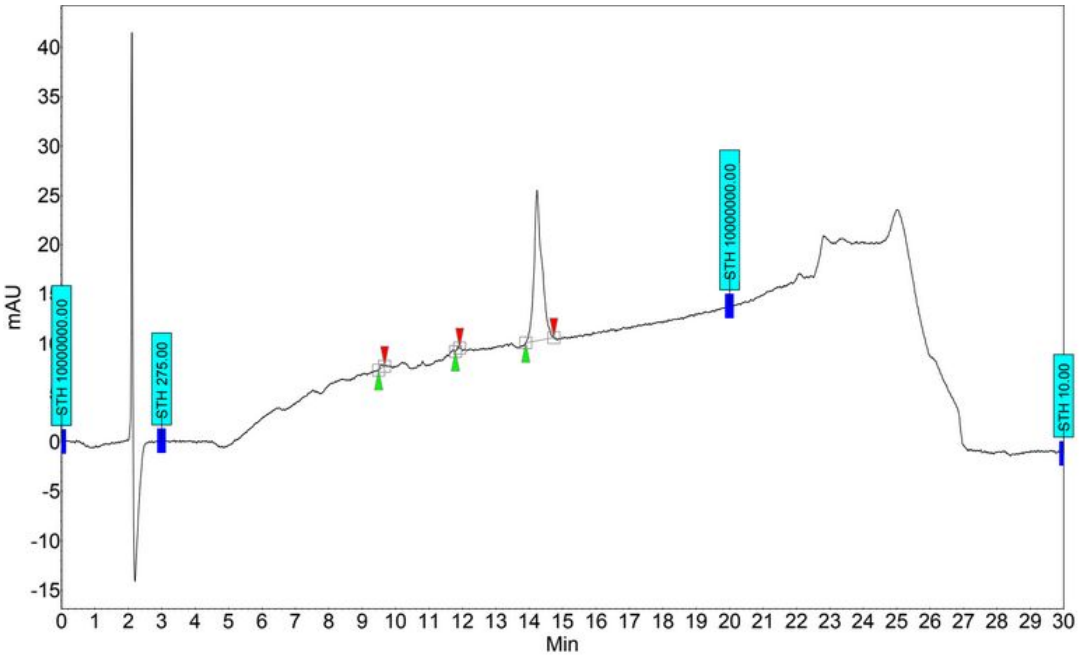

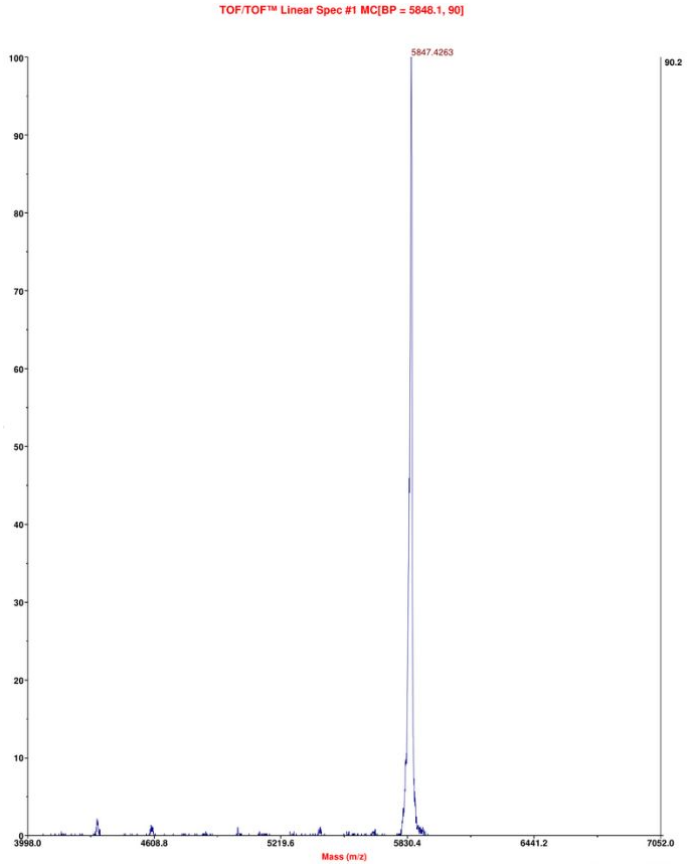

HPLC (5-95% 20 min) RT = 14.23 min
MALDI-TOF calc. $(M+H)^+$ 5855.85, obs. = 5848.1

L006 loopoid strand

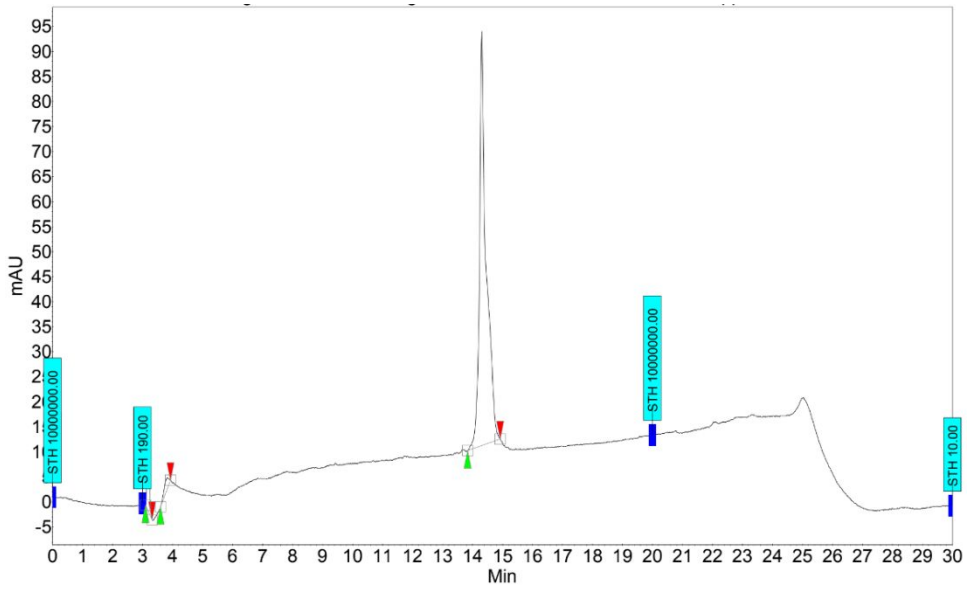

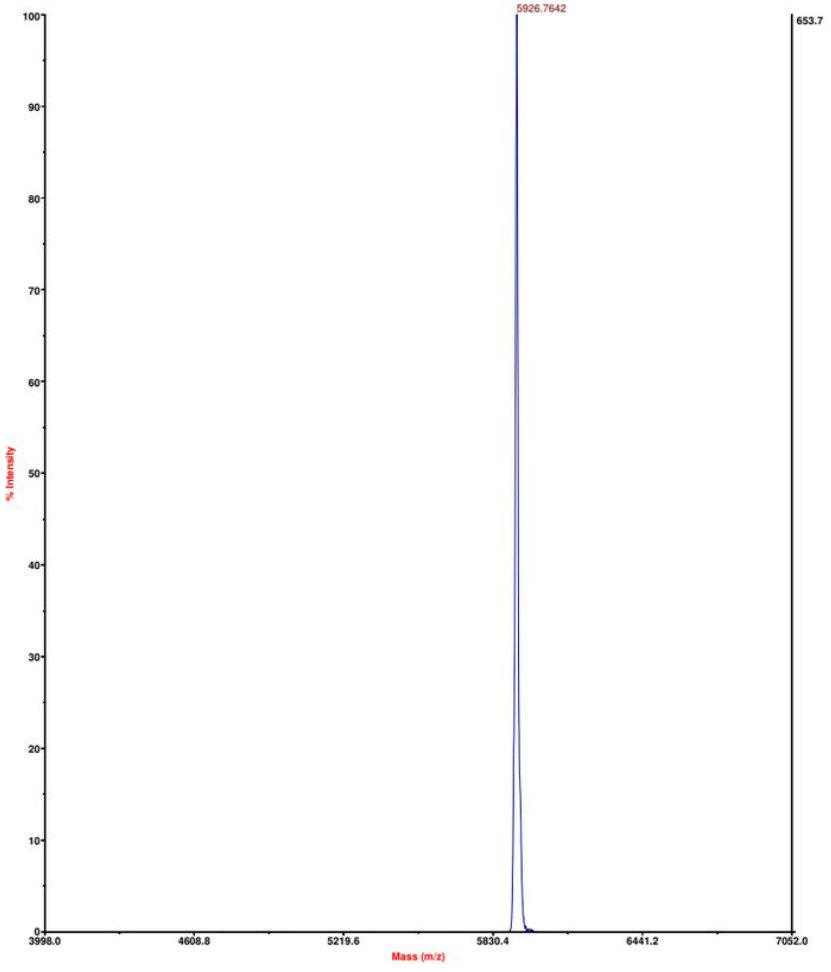

HPLC (5-95% 20 min) RT = 14.31 min
MALDI-TOF calc. $(M+H)^+$ 5932.93, obs. = 5927.8

L009 loopoid strand

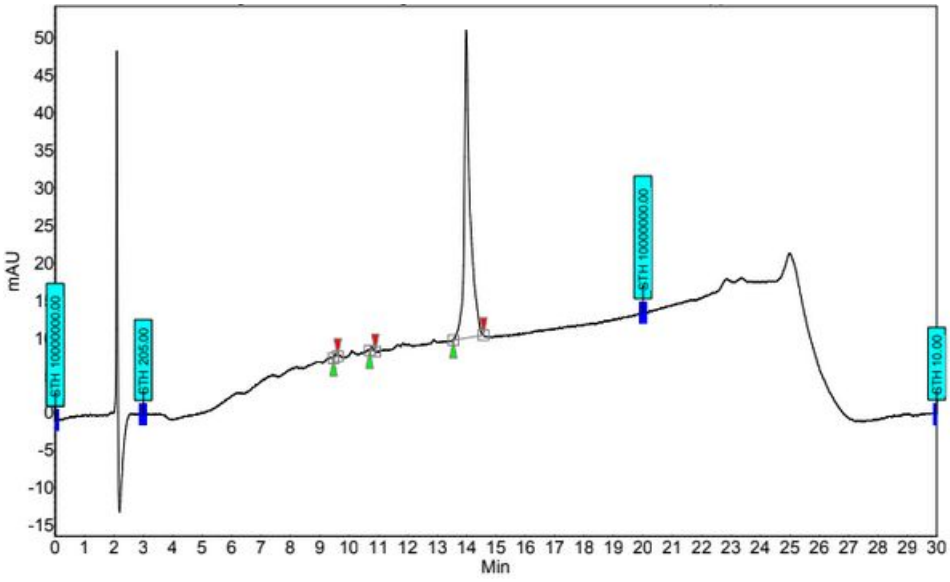

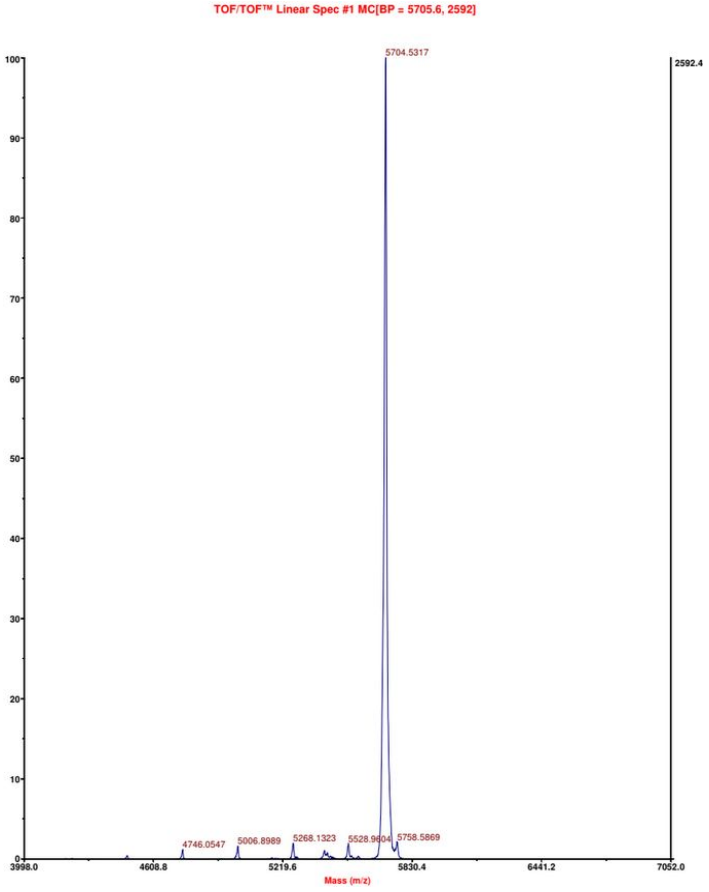

HPLC (5-95% 20 min) RT = 13.99 min
MALDI-TOF calc. $(M+H)^+$ 5710.64, obs. = 5705.6

L011 loopoid strand

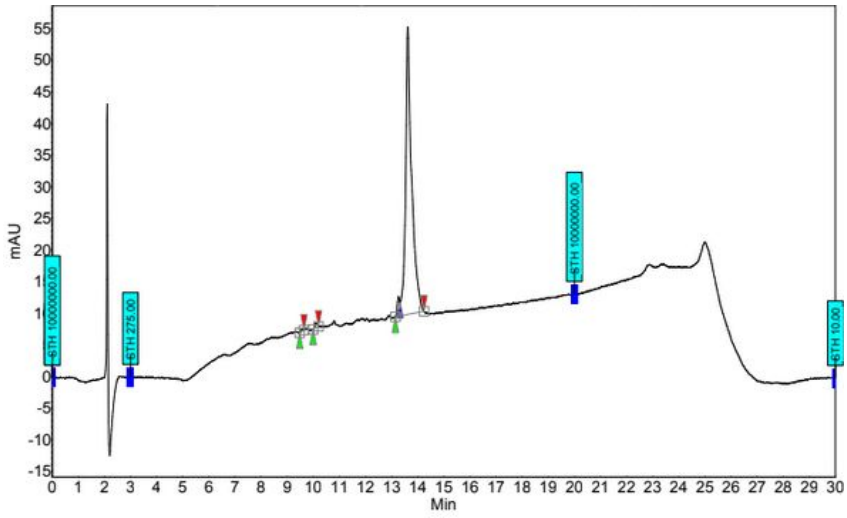

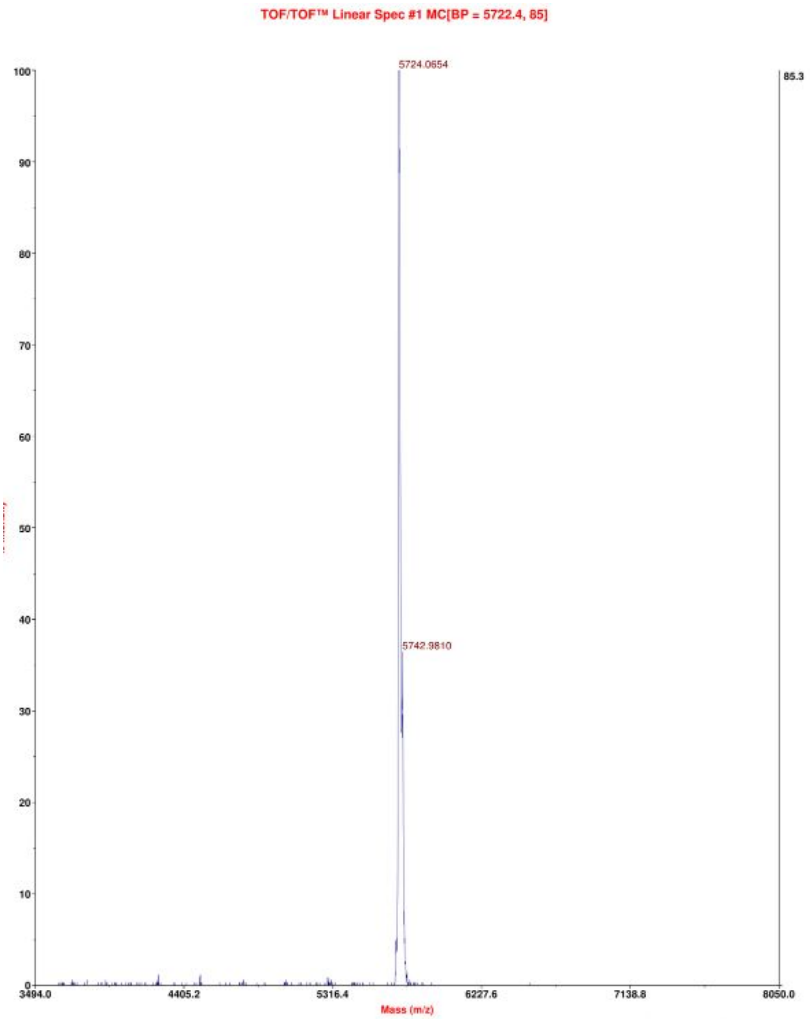

HPLC (5-95% 20 min) RT = 13.61 min
MALDI-TOF calc. $(M+H)^+$ 5939.68, obs. = 5722.4

L034 loopoid strand

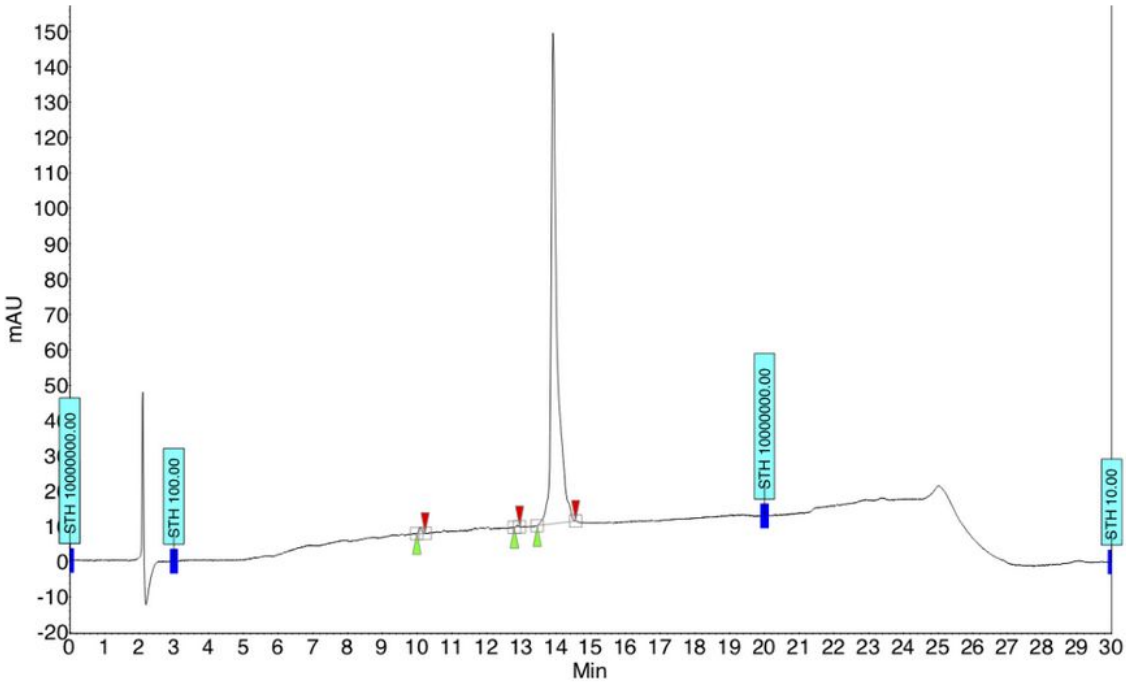

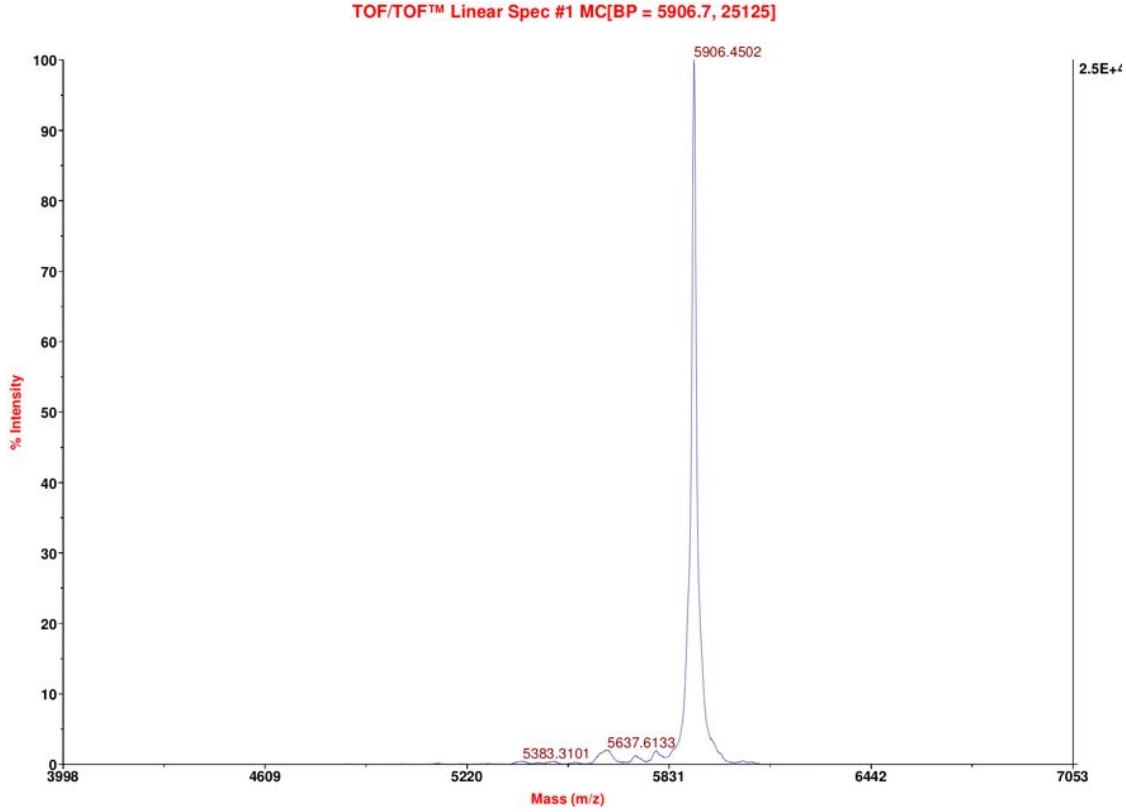

HPLC (5-95% 20 min) RT = 13.91 min
MALDI-TOF calc. $(M+H)^+$ 5919.85, obs. = 5906.45

TYWWLD Peptide

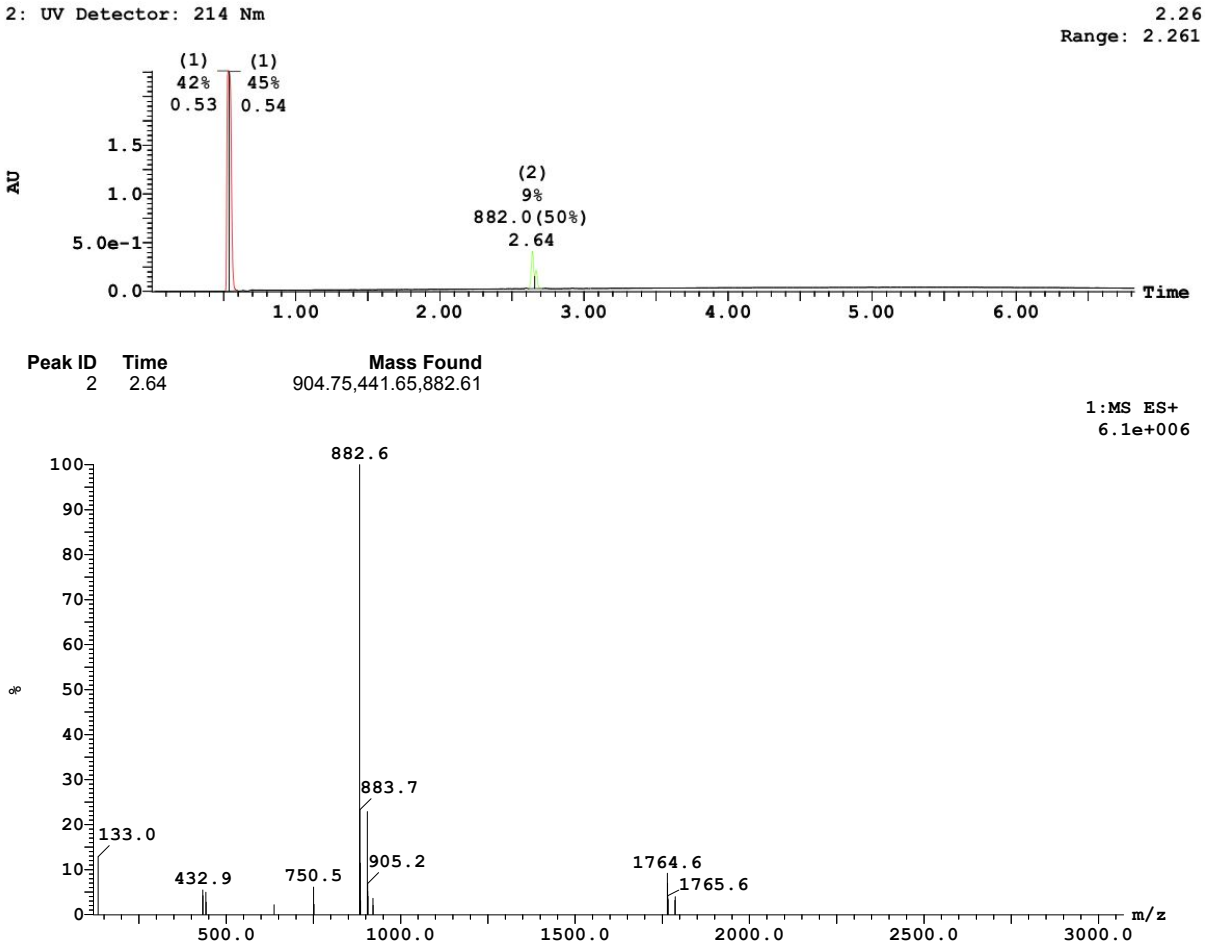

UPLC (5-95% 6.8 min) RT = 2.64 min

ESI-MS calc. $(M+H)^+$ = 882.97, obs. = 882.6

Table S1. HP pattern, sequence, characterization of loopoids

+ and - indicates pass and fail, respectively.

n.a. means that loopoid was not applied to synthesis or test for nanosheet formation.

Abbreviations of monomers are as like below.

Nab: Aminobutyl, Nae: Aminoethyl, Nce: Carboxyethyl, Ncm: Carboxymethyl, Namd: Carboxamide, Nhe: Hydroxyethyl, Npp: Propylpyrrolidinone, Nipr: Isopropyl, Ncpr: Cyclopropylmethy, Nbu: N-butyl, Nia: Isoamyl, Ncpe: Cyclopentyl, Ndpe: Diphenylethyl, Nfu: Furfurylamine, Nph: Phenyl, Npe: Phenylethyl, Nbsa: Benzenesulfonamide, Ntyr: Tyramine, Ntrp: Tryptamine, Npip: Piperonyl

ID	HP pattern	Sequence	M. W.	MALDI (MH+)	Purity	Purified wt. /mg	Nanosheet formation
1	HPPHPP	Ndpe-Ncm-Ncm-Ndpe-Ncm-Ncm	5916.783	1480.17 (4H+)	95+%	39	+
2		Ncpe-Nce-Nce-Ncpe-Npp-Npp	5854.845	5847.4263	95+%	18	+
3		Nbn-Ncm-Nab-Nipr-Ncm-Ncm	5701.576	5688.0205	95+%	33	+
4	PHHPPP	Nab-Ntrp-Ntrp-Nab-Nab-Nab	5895.009	5890.1978	95+%	30	+
5		Ncm-Ndpe-Ndpe-Nhe-Nhe-Ncm	5888.817	1472.90(4H+)	95+%	39	+
6		Npp-Nia-Ntrp-Nce-Nce-Npp	5931.931	5926.7642	90+%	25	+
7	PHPPHP	Namd-Ndpe-Namd-Namd-Ndpe-Namd	5912.847	5907.7891	95+%	13	+
8		Nab-Ndpe-Nab-Nab-Ndpe-Namd	5955.06	1489.47(4H+)	90+%	20	+
9		Nce-Nbu-Nae-Nce-Nia-Nce	5709.64	5704.5317	95+%	30	+
10	PPHHPP	Npp-Npp-Ncpr-Ncpr-Npp-Npp	5933.007	5930.852 (M+H)+	95+%	23	-
11		Nhe-Nae-Ntyr-Ntyr-Nhe-Nae	5738.685	5724.0654	95+%	22	+
12		Npp-Npp-Ntrp-Ncpe-Nab-Nab	5928.035	5922.5142	95+%	26	+
13	HHPHPP	Nipr-Nipr-Nab-Nipr-Nab-Nab	5663.751	5659.6748	95+%	28	-
14		Nipr-Nipr-Nce-Nipr-Nae-Nce	5637.577	95+%	95+%	80	+
15		Nia-Nfu-Ncm-Nfu-Npp-Ncm	5795.689	5792.328 (M+H)+	85+%	18	+
16	HHPPHP	Nbu-Nbu-Npp-Npp-Nbu-Npp	5867.976	5865.745 (M+H)+	95+%	21	-
17		Nbsa-Nbsa-Npp-Npp-Nbsa-Namd	6181.208	6176.3267	95+%	28	+
18		Nbsa-Ncpr-Namd-Nhe-Ncpr-Nhe	5760.706	5754.2998	95+%	18	+
19	HHPPPH	Ncpr-Ncpr-Npp-Npp-Npp-Ncpr	5861.928	1466.59(4H+)	95+%	43	+
20		Ncpr-Ncpr-Nab-Npp-Nab-Ncpr	5753.832	5748.436	95+%	24	+
21		Ncpe-Nfu-Nab-Nab-Namd-Nfu	5751.728	5739.7236	95+%	28	+
22	HPHHPP	Ntrp-Namd-Ntrp-Ntrp-Namd-Namd	5924.862	5920.917	95+%	11	+
23		Nipr-Nab-Nipr-Nipr-Npp-Nab	5717.799	5705.4771	93%	15	+
24		Nipr-Nce-Nbu-Nbu-Nae-Nae	5636.637	5634.1123	95+%	16	+
25	PHHHPP	Nae-Ncpe-Ncpe-Ncpe-Nae-Nae	5657.703	943.77(6H+)	95+%	82	+
26		Npp-Npip-Npip-Npip-Npp-Npp	6102.054	1528.08(4H+)	95+%	52	+
27		Namd-Nipr-Nipr-Npip-Npp-Npp	5849.829	1463.22(4H+)	90+%	51	+
28	PHHPHP	Nae-Ncpr-Ncpr-Nae-Ncpr-Nae	5615.622	1404.86(4H+)	90+%	14	+
29		Nhe-Nipr-Nipr-Nce-Nipr-Nce	5638.561	1410.48(4H+)	85+%	18	+
30		Nhe-Nbu-Nia-Nhe-Nia-Npp	5733.794	1433.9 (M+4H)4+	90+%	22	+
31	PPPHHH	Nce-Nce-Nce-Npip-Npip-Npip	5942.73	1189.34(5H+)	95+%	62	+
32		Nhe-Nhe-Npp-Nia-Nia-Nia	5747.821	5745.711 (M+H)+	90+%	17	-
33		Npp-Nhe-Nhe-Ndpe-Ndpe-Npe	6002.068	1501.33(4H+)	95+%	28	+
34	PHHHHP	Namd-Ntyr-Ntyr-Ntyr-Ntyr-Namd	5918.847	5904.1196	95+%	36	+
35		Npp-Nbu-Nbu-Nbu-Nbu-Namd	5730.794	1432.9 (M+4H)4+	90+%	3	+
36		Ncm-Ncpr-Npip-Ncpr-Npip-Npp	5883.798	5879.6567	90+%	13.9	+

ID	HP pattern	Sequence	M. W.	MALDI (MH+)	Purity	Purified wt. /mg	Nanosheet formation
37	HPHPPP	Ndpe-Ncm-Ncm-Ndpe-Ncm-Ncm	5908.985	1477.85 [M+4H]	95%	25	+
38		Ncpe-Nce-Nce-Ncpe-Npp-Npp	6149.205	6135.4141 [M+H]+	95%	10	+
39		Nbn-Ncm-Nab-Nipr-Ncm-Ncm	6005.076	1201.9 (M+5H)5+	90+%	12	-
40	HPPPPH	Nab-Ntrp-Ntrp-Nab-Nab-Nab	5640.621	1411.0 (M+4H)4+	95+%	18	n.a.
41		Ncm-Ndpe-Ndpe-Nhe-Nhe-Ncm	5678.626	5669.4976 [M+H]+	95%	23	+
42		Npp-Nia-Ntrp-Nce-Nce-Npp	5759.568	5751.0220 [M+H]+	95+%	16	+
43	PHPHPP	Namd-Ndpe-Namd-Namd-Ndpe-Namd	5664.467	1416.71 [M+4H]	95%	22	+
44		Nab-Ndpe-Nab-Nab-Ndpe-Namd	5780.902	1446.0 (M+4H)4+	95+%	10	-
45		Nce-Nbu-Nae-Nce-Nia-Nce	5642.604	5630.5684 [M+H]+	90+%	17	-
46	PHPPPH	Npp-Npp-Ncpr-Ncpr-Npp-Npp	5604.599	1121.76 [M+5H]	85%	50	-
47		Nhe-Nae-Ntyr-Ntyr-Nhe-Nae	5756.699	1439.9 (M+4H)4+	95%	17	+
48		Npp-Npp-Ntrp-Ncpe-Nab-Nab	5815.727	1454.73 [M+4H]	70%	9	+
49	PPPHHP	Nipr-Nipr-Nab-Nipr-Nab-Nab	5902.985	1476.9 (M+4H)4+	n.a.	n.a.	-
50		Nipr-Nipr-Nce-Nipr-Nae-Nce	5698.58	1425.34 [M+4H]	50%	10	+
51		Nia-Nfu-Ncm-Nfu-Npp-Ncm	5954.965	1489.32 [M+4H]	95+%	44	+
52	HHHPPP	Nbu-Nbu-Npp-Npp-Nbu-Npp	5847.949	5841.3472 [M+H]+	95%	6	+
53		Nbsa-Nbsa-Npp-Npp-Nbsa-Namd	5887.922	---	n.a.	n.a.	n.a.
54		Nbsa-Ncpr-Namd-Nhe-Ncpr-Nhe	5778.658	5769.9619 [M+H]+	95+%	13	+
55	HPPHHP	Ncpr-Ncpr-Npp-Npp-Npp-Ncpr	5666.571	1417.1 (M+4H)4+	90+%	25	-
56		Ncpr-Ncpr-Nab-Npp-Nab-Ncpr	5665.682	1417.08 [M+4H]	95+%	54	-
57		Ncpe-Nfu-Nab-Nab-Namd-Nfu	5769.61	5764.9434 [M+H]+	95%	8	+
58	HPPHPH	Ntrp-Namd-Ntrp-Ntrp-Namd-Namd	5967.075	5987.4419 [M+Na]+	90+%	14	-
59		Nipr-Nab-Nipr-Nipr-Npp-Nab	5711.795	1428.9 (M+4H)4+	95+%%	20	+
60		Nipr-Nce-Nbu-Nbu-Nae-Nae	5810.766	5802.439 [M+H]+	95+%	19	+
61	PHHPPH	Nae-Ncpe-Ncpe-Ncpe-Nae-Nae	5904.009	1476.57 [M+4H]	95+%	57	+
62		Npp-Npip-Npip-Npip-Npp-Npp	5833.789	1459.0 (M+4H)4+	n.a.	n.a.	n.a.
63		Namd-Nipr-Nipr-Npip-Npp-Npp	5744.6	5735.6455 [M+H]+	95+%	9	+
64	PPHHHP	Nae-Ncpr-Ncpr-Nae-Ncpr-Nae	5702.604	1426.46 [M+4H]	95+%	67	+
65		Nhe-Nipr-Nipr-Nce-Nipr-Nce	5680.6	1424.8 (M+4H)4+	90%	16	n.a.
66		Nhe-Nbu-Nia-Nhe-Nia-Npp	5680.598	5672.7271 [M+H]+	95+%	29	-
67	PPHHPH	Nce-Nce-Nce-Npip-Npip-Npip	5882.913	5890.3662 [M+Na]+	95+%	20	-
68		Nhe-Nhe-Npp-Nia-Nia-Nia	5900.828	1475.52 [M+4H]	95+%	66	+
69		Npp-Nhe-Nhe-Ndpe-Ndpe-Npe	5955.909	1489.9 (M+4H)4+	90%	20	-
70	PPHPHH	Namd-Ntyr-Ntyr-Ntyr-Ntyr-Namd	5768.754	1443.0 (M+4H)4+	n.a.	n.a.	n.a.
71		Npp-Nbu-Nbu-Nbu-Nbu-Namd	5782.646	1446.34 [M+4H]	---	41	+
72		Ncm-Ncpr-Npip-Ncpr-Npip-Npp	5920.951	1480.77 [M+4H]	---	60	-

ID	HP pattern	Sequence	M. W.	MALDI (MH+)	Purity	Purified wt. /mg	Nanosheet formation
73	HHPPPP	Ndpe-Ncm-Ncm-Ndpe-Ncm-Ncm	5634.621	1409.96 [M+4H]	95+%	80	-
74		Ncpe-Nce-Nce-Ncpe-Npp-Npp	5756.656	1440.41 [M+4H]	95+%	57	+
75		Nbn-Ncm-Nab-Nipr-Ncm-Ncm	5913.87	1479.0 [M+4H]4+	90%	30	n.a.
76	HPPPHP	Nab-Ntrp-Ntrp-Nab-Nab-Nab	5694.673	1424.89 [M+4H]	95%	35	+
77		Ncm-Ndpe-Ndpe-Nhe-Nhe-Ncm	5628.663	1408[M+4H]4+	95%	30	n.a.
78		Npp-Nia-Ntrp-Nce-Nce-Npp	5672.5532	n.a.	n.a.	n.a.	n.a.
79	PPHPHP	Namd-Ndpe-Namd-Namd-Ndpe-Namd	5750.871	1438.09 [M+4H]	90%	27	n.a.
80		Nab-Ndpe-Nab-Nab-Ndpe-Namd	5747.6228	n.a.	n.a.	n.a.	n.a.
81		Nce-Nbu-Nae-Nce-Nia-Nce	5907.91	1478.49 (M+4H)4+	85%	5	+
82	PPHPPH	Npp-Npp-Ncpr-Ncpr-Npp-Npp	6028.9764	n.a.	n.a.	n.a.	n.a.
83		Nhe-Nae-Ntyr-Ntyr-Nhe-Nae	5974.955	5962.3091 [M+H]+	90%	12	+
84		Npp-Npp-Ntrp-Ncpe-Nab-Nab	5945.1118	1487.45 (M+4H)4+	90%	25	+
85	PPPHPH	Nipr-Nipr-Nab-Nipr-Nab-Nab	6057.2445	1515.97 (M+4H)4+	90%	10	n.a.
86		Nipr-Nipr-Nce-Nipr-Nae-Nce	5701.576	1426.16 [M+4H]	95+%	26	n.a.
87		Nia-Nfu-Ncm-Nfu-Npp-Ncm	5758.6862				n.a.
88	PPPPHH	Nbu-Nbu-Npp-Npp-Nbu-Npp	5809.672	1453.0 (M+4H)4+	<85%	5	n.a.
89		Nbsa-Nbsa-Npp-Npp-Nbsa-Namd	5854.7284	n.a.	n.a.	n.a.	n.a.
90		Nbsa-Ncpr-Namd-Nhe-Ncpr-Nhe	5678.582	1420.16 [M+4H]	90%	29	n.a.
91	HPHPPH	Ncpr-Ncpr-Npp-Npp-Npp-Ncpr	5758.76	1440.26 [M+4H]	95%	46	n.a.
92		Ncpr-Ncpr-Nab-Npp-Nab-Ncpr	5769.746	n.a.	n.a.	n.a.	n.a.
93		Ncpe-Nfu-Nab-Nab-Namd-Nfu	5711.6762	n.a.	n.a.	n.a.	n.a.
94	HPPPHH	Ntrp-Namd-Ntrp-Ntrp-Namd-Namd	6017.004	n.a.	n.a.	n.a.	n.a.
95		Nipr-Nab-Nipr-Nipr-Npp-Nab	5944.827	5931.6548 [M+H]+	90%	14	+
96		Nipr-Nce-Nbu-Nbu-Nae-Nae	5693.648	5684.2407 [M+H]+	92%	14	+
97	PHPHHP	Nae-Ncpe-Ncpe-Ncpe-Nae-Nae	5679.746	1420.76 [M+4H]	95%	43	n.a.
98		Npp-Npip-Npip-Npip-Npp-Npp	5699.738	1425.9 [M+4H]+	95%	12	n.a.
99		Namd-Nipr-Nipr-Npip-Npp-Npp	5792.681	n.a.	n.a.	n.a.	n.a.
100	PHPPHH	Nae-Ncpr-Ncpr-Nae-Ncpr-Nae	5629.605	1408.16 [M+4H]	80%	9	n.a.
101		Nhe-Nipr-Nipr-Nce-Nipr-Nce	5907.911	1477.9 [M+4H]4+	87-89%	10	n.a.
102		Nhe-Nbu-Nia-Nhe-Nia-Npp	5717.707	1430.29 [M+4H]	80%	7	n.a.
103	HPHPHP	Nce-Nce-Nce-Npip-Npip-Npip	5645.5708	5634.0264 [M+H]+	85%	9	n.a.
104		Nhe-Nhe-Npp-Nia-Nia-Nia	5853.86	5845.3564 [M+H]+	94%	14	+
105		Npp-Nhe-Nhe-Ndpe-Ndpe-Npe	5775.884	n.a.	n.a.	n.a.	+
106	HHPPHH	Namd-Ntyr-Ntyr-Ntyr-Ntyr-Namd	5682.753	1421.44 [M+4H]	95%	45	-
107		Npp-Nbu-Nbu-Nbu-Nbu-Namd	5993.149	1499.15 [M+4H]	95%	49	-
108		Ncm-Ncpr-Npip-Ncpr-Npip-Npp	5724.839	1431.9 [M+4H]4+	90%	24	-

ID	HP pattern	Sequence	M. W.	MALDI (MH+)	Purity	Purified wt. /mg
109	HPPHPP	Nipr-Nhe-Nhe-Ncpe-Nhe-Nhe	5610.551	1403.88 [M+4H]	95%	2
110		Nph-Namd-Namd-Ncpr-Ncm-Ncm	5684.51	n.a.	n.a.	n.a.
111		Nipr-Nmp-Nmp-Ntrp-Nab-Nce	5866.819	5855.0308 [M+H]+	93%	15
112	PHHPPP	Npp-Ncpe-Ntyr-Npp-Npp-Npp	6013.093	7155.413 [M+H]+	95+%	24
113		Npp-Nbsa-Nia-Nae-Nae-Npp	5913.98	1183.9 [M+4H]4+	95%	17
114		Nab-Nph-Nfu-Nmp-Npp-Nab	5854.852	5843.3057 [M+H]+	92%	28
115	PHPPHP	Ncm-Nia-Ncm-Ncm-Nipr-Ncm	5668.499	1418.06 [M+4H]	90%	26
116		Namd-Ncpr-Namd-Nae-Ncpe-Nae	5646.5616	n.a.	n.a.	n.a.
117		Nae-Npe-Nae-Ncm-Nia-Nme	5700.68	1426.24 [M+4H]	90%	42
118	PPHHPP	Nhe-Nhe-Ndpe-Ncpr-Nhe-Nhe	5734.693	1434.49 [M+4H]	95%	5
119		Nce-Nce-Nipr-Nph-Namd-Namd	5700.55	n.a.	n.a.	n.a.
120		Npp-Nab-Ncpr-Ntyr-Nce-Npp	5891.91	5877.7261 [M+H]+	95%	24
121	HHPHPP	Ntyr-Nipr-Nme-Nipr-Nme-Nme	5702.692	5695.7388 [M+H]+	95%	28
122		Nia-Ntyr-Nae-Ntyr-Nce-Nce	5821.771	5819.2891 [M+H]+	95%	36
123		Ndpe-Ndpe-Nce-Ncpr-Namd-Nae	5910.92	n.a.	n.a.	n.a.
124	HHPPHP	Ntrp-Ncpr-Nme-Nme-Ncpr-Nme	5749.752	n.a.	n.a.	n.a.
125		Nbu-Nbu-Namd-Ncm-Ndpe-Ncm	5789.729	1448.44 [M+4H]	90%	9
126		Nspe-Nspe-Npp-Nce-Nbu-Nab	5842.93	n.a.	n.a.	n.a.
127	HHPPPH	Npip-Nbu-Nce-Nce-Nce-Npip	5864.704	1467.12 [M+4H]	90%	42
128		Ndpe-Ncpr-Nab-Ncm-Ncm-Ndpe	5925.926	1482.35 [M+4]	90%	18
129		Nipr-Nspe-Nme-Nab-Nmp-Nipr	5747.78	5739.9175 [M+H]+	95%	35
130	HPHHPP	Ntrp-Nme-Ntrp-Nfu-Nme-Nme	5864.8309	n.a.	n.a.	n.a.
131		Ndpe-Nae-Nipr-Nipr-Nae-Npp	5799.86	1450.77 [M+4H]	95%	26
132		Nfu-Ncm-Nfu-Nspe-Nhe-Nhe	5762.66	n.a.	n.a.	n.a.
133	PHHHPP	Ncm-Nbn-Ncpe-Nbn-Ncm-Ncm	5746.616	1437.64 [M+4H]	90%	16
134		Namd-Ncpr-Ncpr-Nph-Nab-Nab	5707.72	n.a.	n.a.	n.a.
135		Nab-Ncpr-Ncpr-Nbn-Ncm-Nhe	5695.66	1424.66 [M+4H]	90%	13
136	PHHPHP	Npp-Nspe-Nbu-Npp-Nspe-Npp	5964.06	n.a.	90%	32
137		Npp-Nipr-Nipr-Nae-Ndpe-Nae	5799.86	1450.92 [M+4H]	90%	20
138		Nmp-Nia-Nia-Namd-Ndpe-Nab	5879.914	5868.7896 [M+H]+	75%	9
139	PPPHHH	Nce-Nce-Nce-Ncpr-Nbsa-Nbsa	5960.87	n.a.	n.a.	n.a.
140		Nae-Nfu-Nae-Nipr-Ncpe-Nipr	5642.6134	5632.5654 [M+H]+	86%	17
141		Nae-Nme-Nce-Nipr-Nipr-Nia	5651.648	1413.93 [M+4H]	90%	48
142	PHHHHP	Nab-Ncpr-Nph-Ncpr-Ncpr-Nab	5704.76	5904.1196	95+%	45
143		Nmp-Npip-Nipr-Npip-Nipr-Namd	5840.7046	1432.9 (M+4H)4+	90+%	49
144		Nae-Ncpe-Ncpr-Ncpr-Nce-Namd	5672.63	5879.6567	90+%	24

ID	HP pattern	Sequence	M. W.	MALDI (MH+)	Purity	Purified wt. /mg
145	HPHPPP	Ncpr-Nce-Ncpr-Nce-Npp-Nce	5773.683	1444.09 [M+4H]	95%	83
146		Nipr-Namd-Nfu-Nab-Nab-Namd	5702.66	n.a.	n.a.	n.a.
147		Nbn-Namd-Nbu-Nae-Nae-Ncm	5671.6	n.a.	n.a.	n.a.
148	HPPPPH	Nph-Namd-Namd-Nfu-Namd-Nph	5727.5486	n.a.	n.a.	n.a.
149		Nfu-Nhe-Nme-Nhe-Nme-Ntyr	5728.6317	5721.6099 [M+H]+	75%	6
150		Npip-Nmp-Nab-Ncm-Ncm-Nia	5822.6868	n.a.	n.a.	n.a.
151	PHPHPP	Npp-Nipr-Nme-Nipr-Npp-Npp	5841.894	1461.64 [M+4H]	95%	56
152		Nmp-Nph-Nae-Nbu-Nae-Nmp	5756.6941	5747.9019 [M+H]+	95%	8
153		Namd-Ncpr-Nce-Nia-Nab-Nab	5719.6962	n.a.	n.a.	n.a.
154	PHPPPH	Ncm-Ndpe-Nhe-Nhe-Ncm-Ndpe	5888.82	n.a.	n.a.	n.a.
155		Npp-Ndpe-Nab-Nab-Npp-Nph	5973.075	n.a.	n.a.	n.a.
156		Nme-Ndpe-Npp-Npp-Nae-Ncpr	5909.972	1478.60 [M+4H]	90%	97
157	PPPHHP	Nme-Nae-Nme-Ndpe-Ndpe-Nae	5886.937	1472.45 [M+4H]	95%	64
158		Nce-Nab-Nce-Nia-Ncpr-Nce	5735.678	1434.71 [M+4H]	95%	55
159		Npp-Npp-Nmp-Ntrp-Nipr-Namd	5923.8836	n.a.	n.a.	n.a.
160	HHHPPP	Nipr-Nipr-Nipr-Ncm-Nhe-Ncm	5610.507	1403.58 [M+4H]	95%	33
161		Nfu-Nipr-Nipr-Nab-Nab-Nce	5702.696	1426.69 [M+4H]	95%	96
162		Ncpr-Npip-Ncpr-Namd-Npp-Nhe	5792.7038	n.a.	n.a.	n.a.
163	HPPHHP	Nbu-Ncm-Nhe-Nbu-Nbu-Ncm	5652.588	1413.93 [M+4H]	90%	60
164		Nipr-Nae-Namd-Nbu-Nipr-Nae	5607.5682	n.a.	n.a.	n.a.
165		Nfu-Nme-Nab-Nspe-Nfu-Nhe	5761.72	n.a.	n.a.	n.a.
166	HPPHPH	Nbsa-Namd-Ncm-Nbsa-Namd-Nbsa	6045.9618	6036.9316 [M+H]+	95%	15
167		Npip-Ncm-Nab-Ncpr-Nab-Ncpr	5766.739	1442.66 [M+4H]	95%	63
168		Nbu-Nae-Npp-Ndpe-Ncm-Nbu	5842.881	1462.02 [M+4H]	95%	51
169	PHHPPH	Npp-Nia-Nia-Nmp-Nmp-Nia	5873.9256	5865.2129 [M+H]+	90%	22
170		Nae-Ncpr-Nspe-Npp-Npp-Nspe	5879.95	1470.9 [M+4H]4+	95%	34
171		Nae-Nspe-Nspe-Ncm-Nhe-Nipr	5719.68	n.a.	n.a.	n.a.
172	PPHHHP	Nhe-Nce-Ncpe-Ncpe-Ncpe-Nce	5716.675	1430.29 [M+4H]	90%	35
173		Nhe-Nme-Nph-Npe-Npe-Nme	5768.75	n.a.	n.a.	n.a.
174		Nme-Namd-Nia-Nbsa-Ncpe-Nce	5832.81	n.a.	n.a.	n.a.
175	PPHHPH	Nmp-Nce-Ncpr-Ncpr-Nce-Ncpr	5737.6246	n.a.	n.a.	n.a.
176		Nme-Ncm-Ntrp-Ncpr-Nme-Ntrp	5838.793	n.a.	n.a.	n.a.
177		Nmp-Nab-Ntyr-Nipr-Nce-Nipr	5778.738	5765.2773 [M+H]+	95%	27
178	PPHPHH	Nab-Ncm-Ncpr-Nab-Ncpr-Ncpr	5686.697	1422.71 [M+4H]	95%	38
179		Nce-Nab-Ntyr-Nab-Nipr-Nipr	5742.7484	5730.5815 [M+H]+	95%	32
180		Nae-Ncm-Nbsa-Namd-Nbsa-Ndpe	6029	n.a.	n.a.	n.a.

ID	HP pattern	Sequence	M. W.	MALDI (MH+)	Purity	Purified wt. /mg
181	HHPPPP	Ncpe-Ncpe-Nae-Nhe-Nae-Nhe	5634.621	1409.81 [M+4H]	90%	45
182		Nbsa-Nbu-Npp-Npp-Nce-Nce	6218.8909	n.a.	90%	35
183		Ndpe-Nia-Nme-Nhe-Nhe-Nhe	5764.763	1442.51 [M+4H]	95%	22
184	HPPPHP	Nipr-Nce-Nce-Nae-Nipr-Nce	5667.559	1417.76 [M+4H]	95%	67
185		Ndpe-Ncm-Ncm-Ncm-Ncpr-Nab	5803.712	1451.89 [M+4H]	90%	60
186		Nph-Ncm-Ncm-Npp-Ncpr-Ncm	5753.5982	n.a.	n.a.	n.a.
187	PPHPHP	Namd-Nce-Ndpe-Nce-Ndpe-Nce	5957.8694	n.a.	n.a.	n.a.
188		Nae-Ncm-Nbsa-Ncm-Nipr-Nae	5751.6501	n.a.	n.a.	n.a.
189		Nab-Nhe-Nia-Nab-Ncpr-Nhe	5678.718	1420.76 [M+4H]	90%	55
190	PPHPPH	Ncm-Ncm-Nia-Ncm-Nme-Nia	5696.597	1425.11 [M+4H]	90%	28
191		Npp-Nae-Nbu-Nae-Npp-Nipr	5758.808	1440.49 [M+4H]	90%	43
192		Nhe-Nhe-Ndpe-Nab-Nhe-Nfu	5787.757	1447.87 [M+4H]	90%	17
193	PPPHPH	Namd-Nae-Namd-Ntrp-Nae-Ntrp	5810.7276	n.a.	n.a.	n.a.
194		Namd-Namd-Nae-Ntyr-Nae-Ndpe	5824.782	5814.7749 [M+H]+	85%	26
195		Nme-Nme-Nme-Nph-Nae-Ncpe	5685.67	n.a.	n.a.	n.a.
196	PPPPHH	Npp-Npp-Nme-Nme-Nfu-Nfu	5850.813	1463.74 [M+4H]	95%	39
197		Nae-Nce-Nce-Nce-Nbu-Ntyr	5759.6458	5751.9385 [M+H]+	95%	34
198		Nme-Nae-Nae-Nme-Ncpr-Ntrp	5723.705	n.a.	n.a.	n.a.
199	HPHPPH	Nipr-Nhe-Nipr-Nhe-Nab-Nipr	5609.611	1403.58 [M+4H]	95%	58
200		Npip-Npp-Npip-Npp-Nab-Nspe	6018.0118	n.a.	n.a.	n.a.
201		Nfu-Nhe-Nbn-Nce-Nce-Nspe	5786.681	n.a.	n.a.	n.a.
202	HPPPHH	Ncpr-Namd-Namd-Nme-Ncpr-Ncpr	5658.5871	n.a.	n.a.	n.a.
203		Ndpe-Nme-Ncm-Nme-Nia-Nia	5818.855	1455.72 [M+4H]	95%	78
204		Ncpe-Namd-Nce-Nce-Npe-Nipr	5739.658	n.a.	n.a.	n.a.
205	PHPHHP	Npp-Ncpr-Npp-Ncpr-Ncpr-Nmp	5843.856	5829.4287 [M+H]+	92%	23
206		Npp-Nph-Npp-Ncpr-Ncpr-Nme	5816.84	n.a.	n.a.	n.a.
207		Nab-Ntyr-Nme-Ncpe-Nipr-Nme	5741.7606	5731.7388 [M+H]+	92%	38
208	PHPPHH	Nce-Ncpr-Namd-Namd-Ncpr-Ncpr	5672.58	n.a.	n.a.	n.a.
209		Nae-Nipr-Namd-Namd-Npip-Nipr	5699.5788	n.a.	n.a.	n.a.
210		Nae-Nbn-Nmp-Nmp-Nspe-Nbu	5831.804	5824.9771 [M+H]+	90%	28
211	HPHPHP	Ncpe-Nab-Ncpe-Nmp-Ncpe-Nab	5777.8218	n.a.	n.a.	n.a.
212		Nspe-Nab-Ntrp-Nce-Nspe-Nab	5889.9274	n.a.	n.a.	n.a.
213		Nipr-Nab-Ntrp-Nab-Nph-Npp	5852.9097	5845.0396 [M+H]+	70%	16
214	HHPPHH	Nipr-Nipr-Namd-Namd-Nipr-Nipr	5606.5372	n.a.	n.a.	n.a.
215		Nfu-Nspe-Ncm-Nab-Npe-Npe	5845.84	n.a.	n.a.	n.a.
216		Ncpr-Npip-Nae-Ncm-Ncpr-Ndpe	5847.812	1463.29 [M+4H]	95%	68

ID	HP pattern	Sequence	M. W.	MALDI (MH+)	Purity	Purified wt. /mg
217		Ndpe-Namd-Namd-Nme-Nme-Ndpe	5910.94	n.a.	n.a.	n.a.
218	HPPPPH	Ncpr-Nce-Npp-Npp-Nce-Ntrp	5917.904	5905.8164 [M+H]+	60%	13
219		Nia-Npp-Nce-Nce-Nce-Ndpe	5915.884	1479.87 [M+4H]	95%	106
220		Nab-Ndpe-Npp-Nab-Ndpe-Npp	6077.227	1519.78 [M+4H]	90%	118
221	PHPPHP	Npp-Nia-Npp-Nae-Nipr-Nae	5772.835	1444.09 [M+4H]	95%	88
222		Nhe-Ndpe-Nab-Nhe-Nbu-Nab	5790.849	1448.52 [M+4H]	95%	110
223		Ncm-Nme-Nfu-Nme-Ncm-Nfu	5716.543	1430.21 [M+4H]	90%	21
224	PPHPPH	Nfu-Nhe-Ncpr-Nhe-Nhe-Npip	5724.5826	n.a.	n.a.	n.a.
225		Nce-Nme-Nph-Nme-Nce-Nspe	5764.68	n.a.	n.a.	n.a.
226		Nipr-Nipr-Nipr-Nmp-Nme-Nme	5673.6244	n.a.	n.a.	n.a.
227	HHHPPP	Ncpr-Ncpr-Ntrp-Nhe-Nae-Nae	5705.6898	n.a.	n.a.	n.a.
228		Nspe-Nia-Npe-Namd-Ncm-Namd	5774.72	n.a.	n.a.	n.a.
229		Nia-Nia-Ncm-Nab-Nia-Ncm	5721.739	1431.64 [M+4H]	95%	16
230	HHPPHP	Nipr-Ntrp-Nae-Nhe-Nipr-Nae	5681.6678	n.a.	n.a.	n.a.
231		Nspe-Ncpe-Nhe-Npp-Nipr-Npp	5832.89	n.a.	n.a.	n.a.
232		Nipr-Namd-Nipr-Nipr-Nme-Namd	5622.57	n.a.	n.a.	n.a.
233	HPHHPP	Npip-Ncm-Ncpr-Ncpr-Nab-Ncm	5753.652	1439.59 [M+4H]	95%	70
234		Nph-Nhe-Ncpr-Nbu-Ncm-Ncm	5638.52	n.a.	n.a.	n.a.
235		Ntyr-Nce-Ntyr-Nhe-Nce-Ntyr	5872.7613	5863.5210 [M+H]+	95%	29
236	HPHPPH	Nipr-Nce-Nipr-Npp-Npp-Nbsa	5913.93	n.a.	n.a.	n.a.
237		Nfu-Nmp-Ndpe-Nmp-Nab-Npip	6003.944	n.a.	n.a.	n.a.
238		Nbsa-Nce-Nab-Nbsa-Nab-Nbsa	6088.12	1218.8 [M+5H]5+	95%	36
239	HPPHPH	Nbu-Namd-Nab-Ndpe-Nab-Ndpe	5940.0122	n.a.	n.a.	n.a.
240		Nph-Namd-Nme-Nph-Nme-Nipr	5691.599	5683.2041 [M+H]+	73%	17
241		Nab-Nipr-Nipr-Ncm-Nipr-Nab	5650.664	1413.71 [M+4H]	90%	51
242	PHHPHP	Ncm-Nbn-Nfu-Ncm-Nbn-Namd	5757.5718	n.a.	n.a.	n.a.
243		Nae-Npip-Ndpe-Nae-Nipr-Ncm	5824.778	1457.29 [M+4H]	95%	92
244		Nae-Ncpr-Namd-Ncpr-Ncpr-Nae	5629.605	1408.46[M+4H]	90%	27
245	PHPHHP	Ncm-Nbu-Nab-Nbu-Ncpr-Ncm	5677.642	1420.31 [M+4H]	90%	64
246		Nab-Nspe-Nab-Ndpe-Nbu-Npp	5932.08	n.a.	n.a.	n.a.
247		Nme-Nme-Ntyr-Ntyr-Namd-Ntyr	5857.804	n.a.	n.a.	n.a.
248	PPHHPH	Nce-Nmp-Ncpe-Nipr-Nmp-Ncpe	5788.7332	5775.3403 [M+H]+	95%	23
249		Nae-Namd-Ncpr-Nph-Namd-Nia	5681.64	n.a.	n.a.	n.a.
250		Ncpe-Ncpe-Namd-Namd-Ncpe-Ncpe	5710.6884	n.a.	n.a.	n.a.
251	HHPPHH	Nipr-Ntyr-Nae-Nce-Ntyr-Nipr	5763.7234	5756.9761 [M+H]+	95+%	40
252		Ncpe-Ncpe-Npp-Nce-Nipr-Nbsa	5882.92	n.a.	n.a.	n.a.
253		Nhe-Ncpr-Ncpr-Ncpr-Ncpr-Npp	5709.731	1428.41 [M+4H]	90%	15
254	PHHHHP	Nmp-Ncpr-Ncpr-Nspe-Ncpr-Nae	5740.7172	n.a.	n.a.	n.a.
255		Namd-Nia-Ntyr-Nia-Nph-Nae	5760.7661	5749.7959 [M+H]+	93%	33
256		Npp-Nspe-Nipr-Nfu-Nfu-Ncm	5813.75	n.a.	n.a.	n.a.

B. SUPPLEMENTARY DATA

Anthrax protective antigen (PA63)7 preparation.

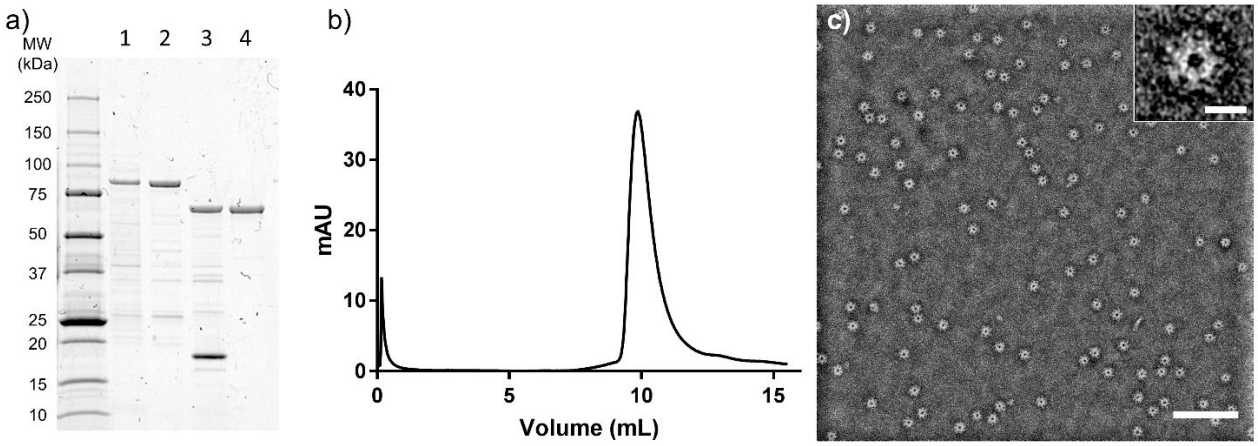

(PA63)7 expression, purification, and characterization. a) SDS-PAGE gel of $(PA63)_7$ at different stages of purification. 1) Soluble whole cell lysate containing PA83, 2) PA83 contained in fraction eluted from anion exchange column, 3) PA63 and PA20 after trypsin cleavage of PA83, 4) $(PA63)_7$ contained in fraction eluted from second round of anion exchange chromatography. b) UV absorbance spectrum (mAU) versus elution volume (mL) from size exclusion chromatography of Alexa Fluor-647 conjugated $(PA63)_7$. c) Survey view of $(PA63)_7$ by transmission electron microscopy with negative staining. Scale bar = 100 nm. Inset in upper right corner shows higher magnification of a representative particle of $(PA63)_7$. Scale bar in inset = 10 nm.

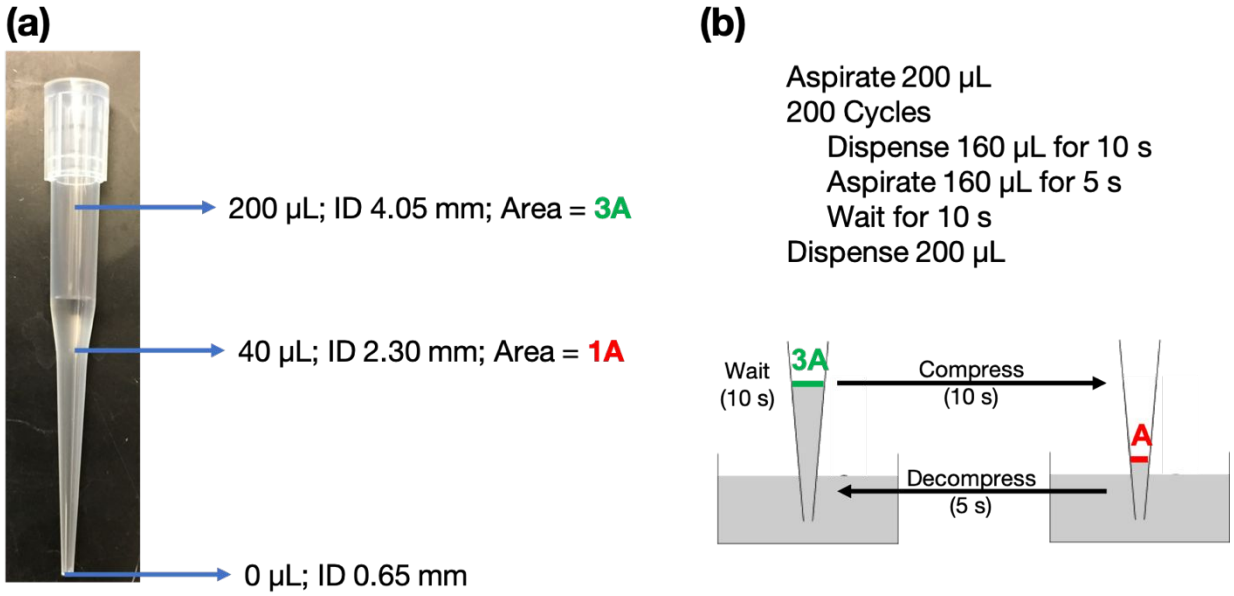

Figure S1. Pipet tip geometry for interfacial compression.

Nanosheets are formed by repeated interfacial compression of a peptoid solution. (a) The inner diameter of a P250 pipet tip defines the air/water interfacial area at different volumes of aspirated liquid. Area compression ratio of 3 can be achieved by changing the volume between the 200 µL and 40 µL positions. (b) The robotic pipettor is programmed to perform 200 compression cycles. By controlling the aspirate and dispense flow rates (32 µL/s and 16 µL/s, respectively) and the post-aspiration wait time (10 s), the peptoid molecules have enough time to re-populate the newly formed air/water interface during each cycle.

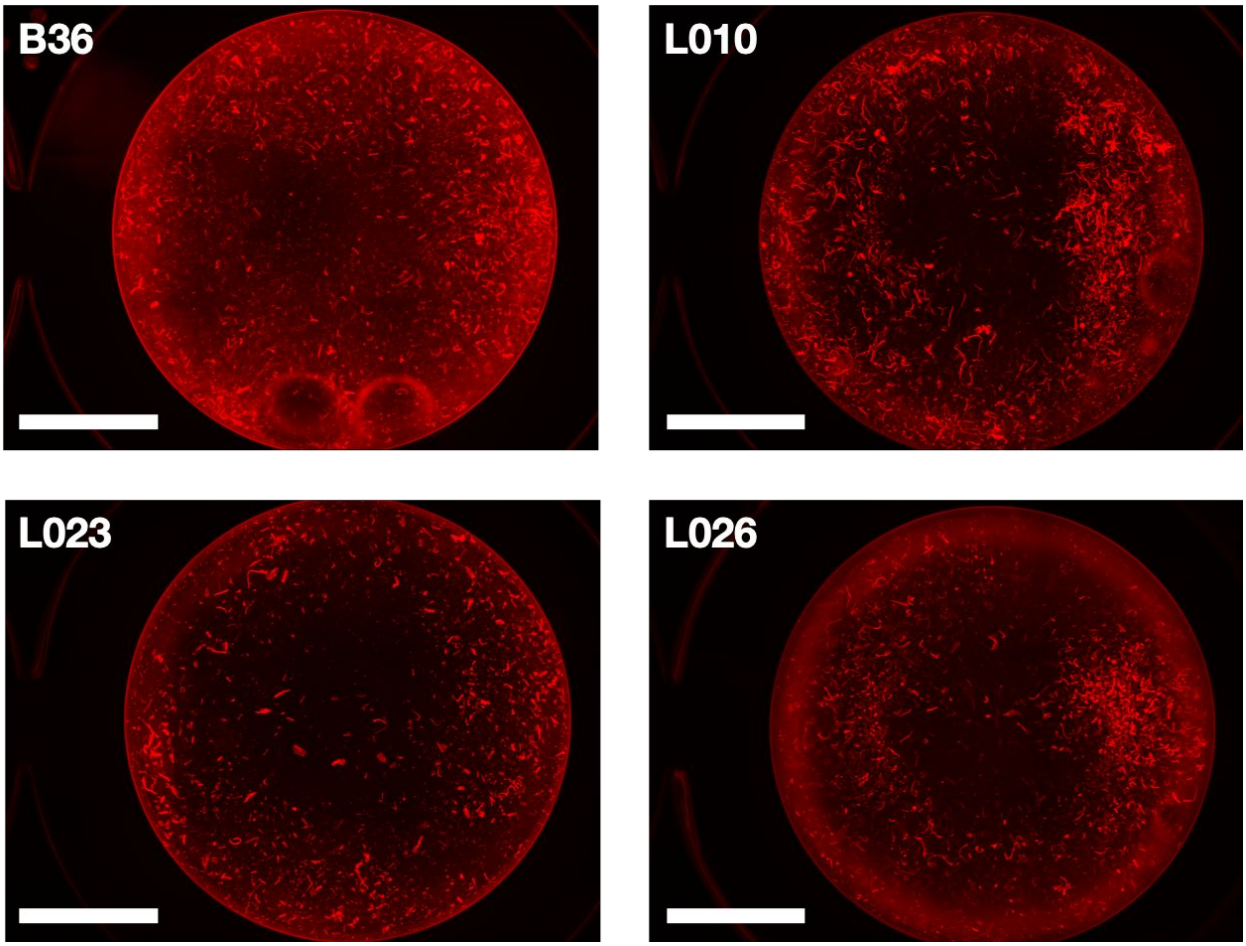

Figure S2. Fluorescence microscopic images of pipet-generated nanosheets.

Representative fluorescence images of nanosheets (loopoid ID's: B36, L010, L023, L026) produced in a 96-well plate produced by the robotic pipetting method. The scale bar is 2 mm.

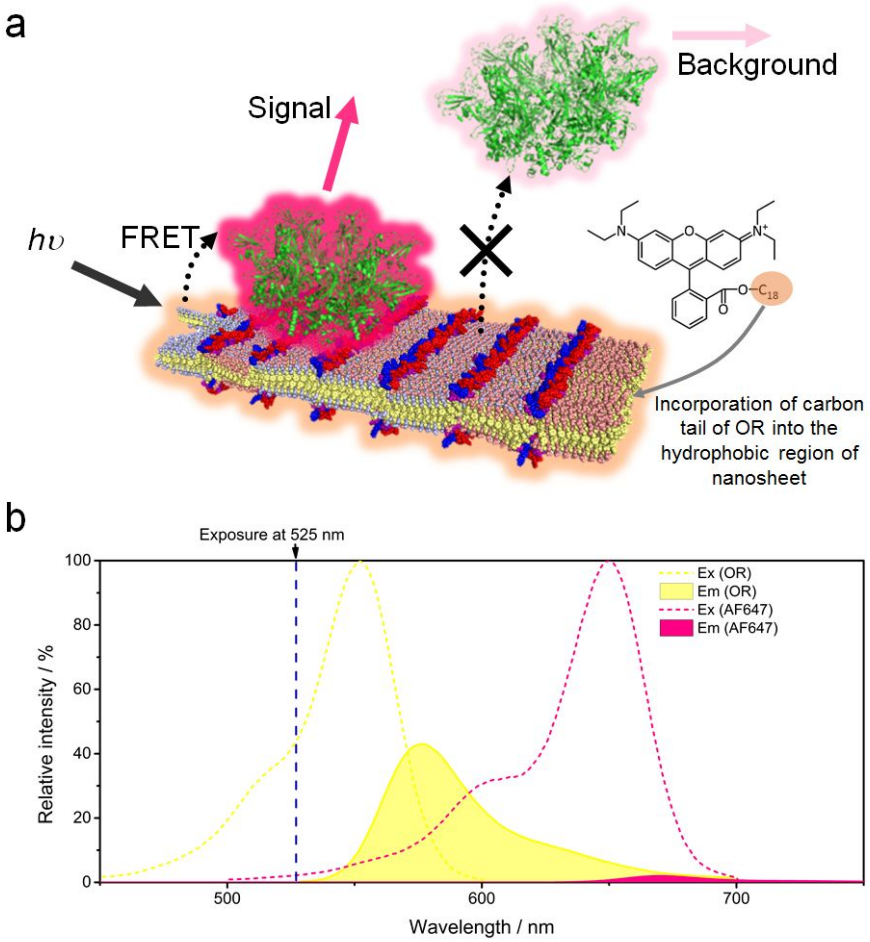

Figure S3. Homogeneous FRET assay for the identification of binding affinity of loopoid nanosheet.

(a) Schematic illustration of FRET assay using the incorporation of octadecyl rhodamine (OR) into nanosheet and Alexa Fluor 647 (AF647)-conjugated protein substrate. Long hydrocarbon chain of OR facilitates insertion into the hydrophobic core of peptoid bilayer. When AF647-conjugated protein is bound on the nanosheet surface, the fluorescence of OR (FRET donor) is transferred into Alexa Fluor 647 (FRET acceptor) via FRET phenomenon. (b) Absorbance (dotted line) and fluorescence (filled area) of OR (yellow) and AF647 (red). The fluorescence emission spectra are normalized to show the relative fluorescence intensities by direct excitation at 525 nm.

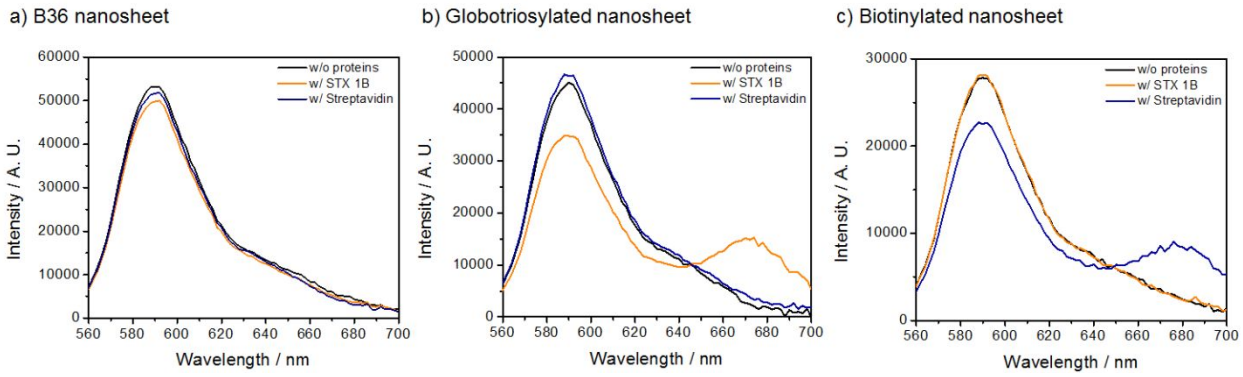

Figure S4. FRET assay to identify protein binding to peptoid nanosheet.

Fluorescence spectra of a) B36, b) globotriosylated, and c) biotinylated nanosheet in the absence (black line) and presence of STX 1B (orange line) and streptavidin (blue line). All spectra were obtained under the excitation wavelength at 525 nm. Globotriose and biotin are binding elements for STX 1B and streptavidin, respectively.

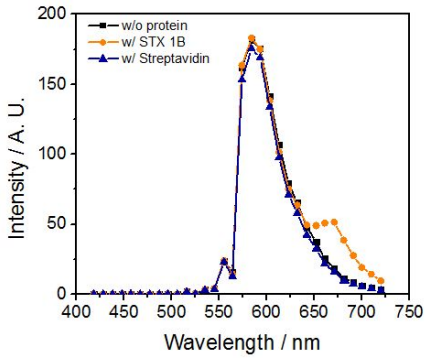

Figure S5. Identification of the origin of FRET signal by confocal microscopy.

Spectra were obtained by spectral scanning of globotriosylated nanosheet in the absence and presence of STX 1B and streptavidin.

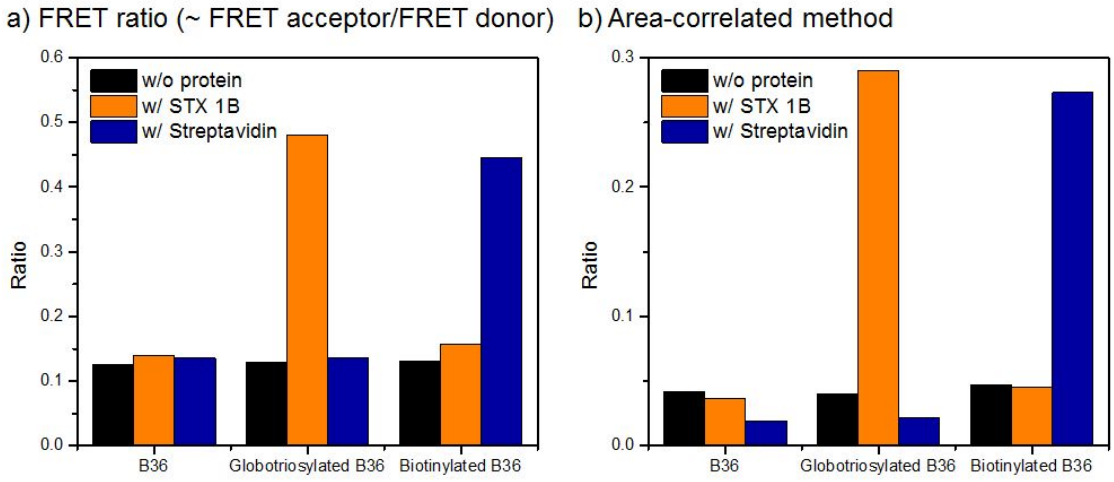

Figure S6. Curve fitting method provides more accurate measure of FRET efficiency.

FRET ratio obtained by a) calculating a simple ratio of donor and acceptor fluorescence intensities ($I_{Alexa647}$ / I_{OR}) and b) curve fitting fluorescence spectra with a linear combination of donor and acceptor emission spectra and calculating the ratio of the regression coefficients.

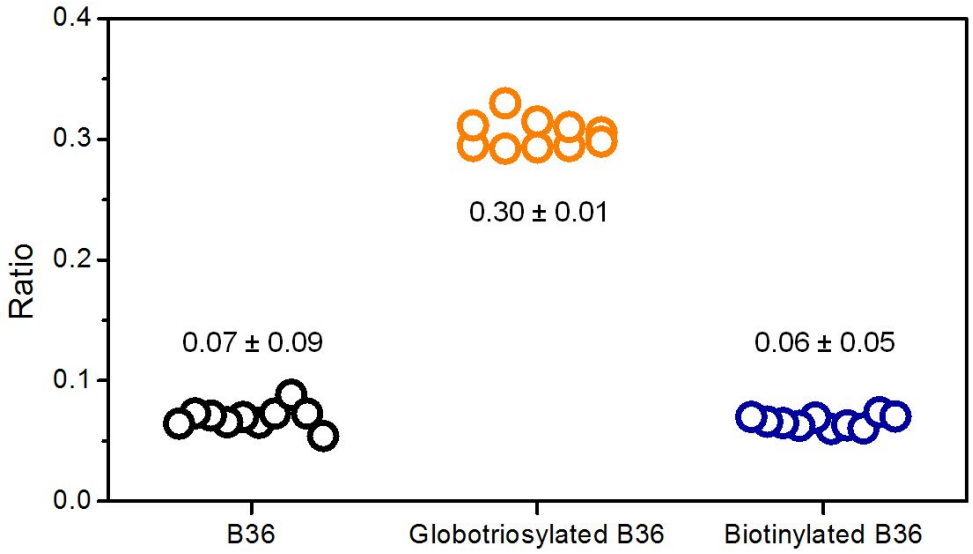

Figure S7. Z-factor calculation validates the reliability of developed FRET assay.

FRET ratio obtained from 10 samples of B36, globotriosylated, and biotinylated nanosheet in the presence of STX 1B. Based on the value of average and standard deviation, Z-factor of our screening assay is approximately 0.73.

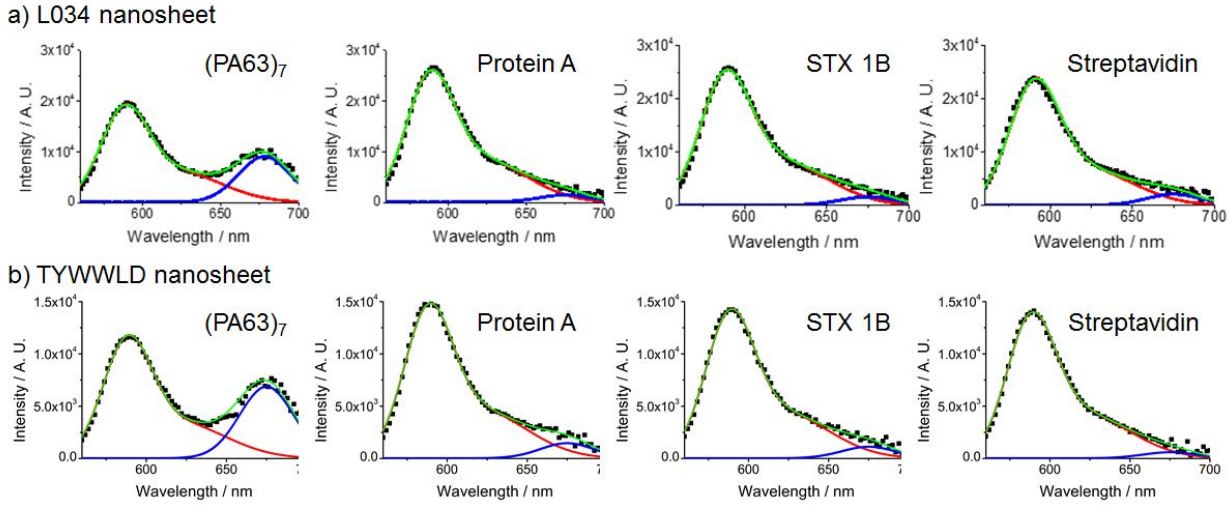

Figure S8. Validation of binding specificity of L034 and TYWWLD nanosheet by FRET assay.

All spectra were obtained under the excitation wavelength at 525 nm with 2 nm interval for data acquisition. By curve fitting using Gaussian function-derived donor and acceptor spectra, the emission spectra can be decomposed into OR (red line) and AF647 (blue line) components. Green line represents the sum of OR and AF647 spectra. All nanosheets were prepared by vial-rocking method. Positive FRET signal is clearly observed only in the presence of $(PA63)_7$.

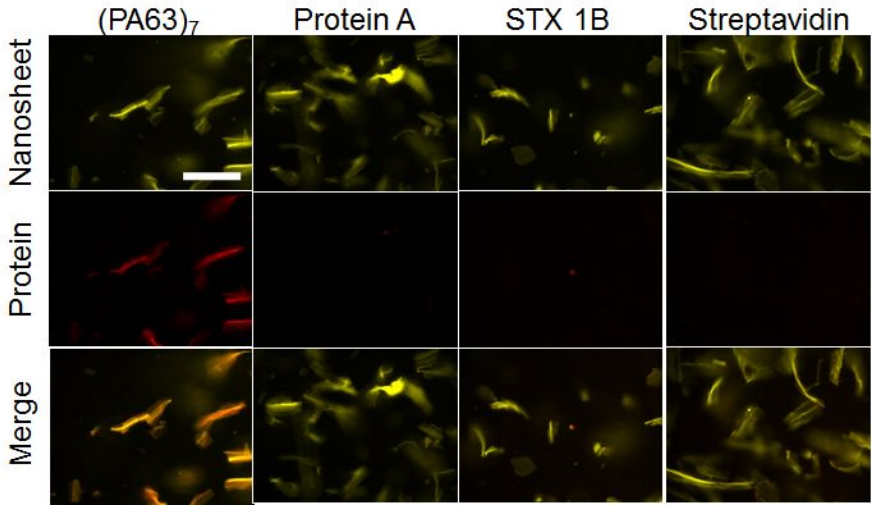

Figure S9. Validation of binding specificity of TYWWLD nanosheet by fluorescent microscopy.

OR-stained nanosheets are visualized with TR filter (yellow color). AF647-conjugated proteins are detected in Cy5 filter (red color). The colocalization of fluorescence signals in the merged image shows the binding specificity of TYWWLD nanosheets. Scale bar represents 100 μm. All images were acquired with the same magnification.

Table S2. Comparison of HP pattern and chemical property of monomers between L034 and TYWWLD loop sequences.

ID	HP pattern		1st	2nd	3rd	4th	5th	6th
L034	**PHHHHP**	Monomer	Namd	Ntyr	Ntyr	Ntyr	Ntyr	Namd
		Chemical property	Hd	**Ar**	**Ar**	**Ar**	Ar	Hd
TYWWLD	**PHHHHP**	Monomer	Thr	Tyr	Trp	Trp	Leu	Asp
		Chemical property	Hd	**Ar**	**Ar**	**Ar**	Sa	An

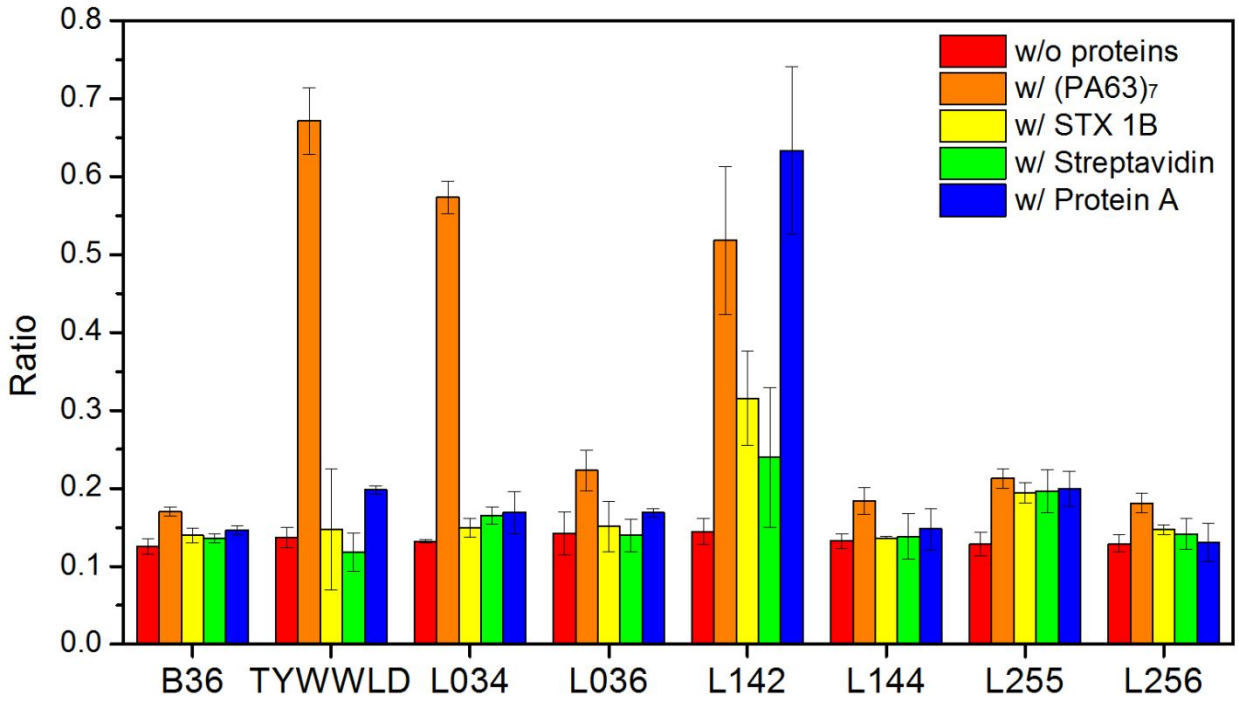

Figure S10. FRET-based validation of protein binding to nanosheets classified as PHHHHP pattern.

Among various nanosheets, only TYWWLD and L034 nanosheets showed high $(PA63)_7$ binding specificity. L142 represents non-specific binding to multiple target proteins.

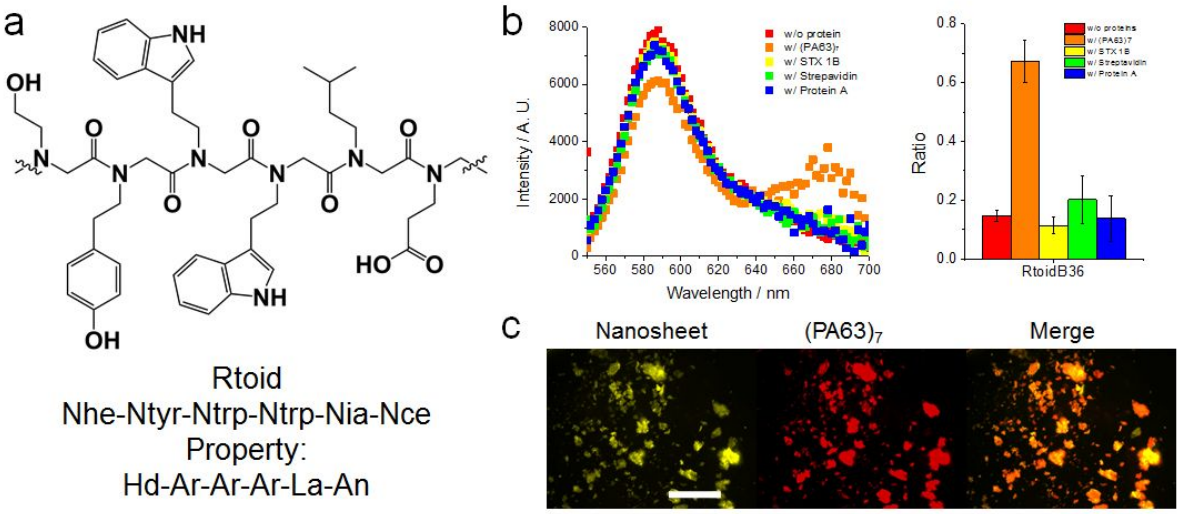

Figure S11. Chemical structure and $(PA63)_7$ binding specificity of Rtoid.

(a) Sequence and chemical property of Rtoid loop. (b) FRET-based validation of selective $(PA63)_7$ binding to Rtoid nanosheet. (c) Fluorescent images of Rtoid nanosheet in the presence of $(PA63)_7$.

Table S3. Binding parameters of B36, TYWWLD, and L034 nanosheet measured by bio-layer interferometry.

	Kd (nM)	k_{on} (M^{-1} s^{-1})	k_{dis} (s^{-1})
B36 nanosheet	-	-	-
TYWWLD nanosheet	1.59	8.71×10^{4}	1.38×10^{-4}
L034 nanosheet	1.95	4.74×10^{4}	9.24×10^{-5}

To obtain all binding parameters, all binding curves (Figure 5a) were fitted with 2:1 binding model. No binding observed in B36 nanosheet.